nature communications

Article

https://doi.org/10.1038/s41467-026-68481-6

Spectroelectrochemical insight into copper cobalt catalysts for CO_2 and nitrite co-electroreduction to urea

Received: 19 May 2025

Accepted: 8 January 2026

Published online: 17 January 2026

Check for updates

Putri Ramadhany[1,2], Thành Trần-Phú[3] ✉, Jodie A. Yuwono[4], Rosalie K. Hocking[3], Zhipeng Ma[1], Xuan Minh Chau Ta[5], Priyank Kumar[1], Denny Gunawan[1], Bernt Johannessen[6,9], Antonio Tricoli[5], Alexandr N. Simonov[7], Rose Amal[1] & Rahman Daiyan[8] ✉

Electrochemical CO_2 and nitrite co-reduction provides a sustainable urea synthesis route but remains limited by low selectivity and an undecided C–N coupling mechanism. Here, we report co-sputtered bimetallic Cu–Co catalysts that facilitate urea formation via a tandem relay mechanism. The optimal Cu:Co ratio of 1:1 achieves a urea yield rate of 61 ± 6 mmol $h^{-1}g_{cat}^{-1}$ at −1.2 V vs. RHE under neutral pH, emphasizing the importance of proton balance in sustaining proton-coupled electron transfer. In situ synchrotron-based infrared and Raman spectroscopy monitor the dynamic evolution of *CO, $*NH_2$, and C–N intermediates. In situ X-ray absorption spectroscopy indicates the structural stability of metallic Cu and Co active sites. Density functional theory calculations suggest that *COOH + $*NH_2$ coupling initiates urea pathway, with $*NH_2CO$ formation as the potential-determining step. This study integrates rational catalyst design and in situ spectroelectrochemical analysis to advance understanding of electrochemical C–N coupling for urea synthesis.

Urea ($CO(NH_2)_2$) is the most utilized fertilizer globally with market size around $129 billion in 2023, which it is projected to grow to around $161 billion by 2032[1]. Currently, the primary method for commercial urea production is the Bosch-Meiser process, which involves the reaction of ammonia (NH_3) and CO_2 under elevated temperature (150–200 °C) and pressure (100–200 bar)[2]. NH_3 is typically derived from the Haber-Bosch process, which relies on hydrogen sourced from fossil fuels, making upstream hydrogen production the main contributor to energy consumption and carbon emissions[2]. As a result, the overall urea production remains carbon-intensive, generating ~910 kg of CO_2 for every ton of urea produced[3,4].

Electrochemical co-reduction of CO_2 and NO_x^-, such as NO_2^- or NO_3^-, offers a promising, more sustainable alternative. These NO_x^- species can be sourced from exhaust flue gas, chemical production by-product, wastewater streams, or synthesized via cold plasma oxidation of N_2[5–10]. Such approaches could enable decentralized and potentially carbon-neutral urea production. However, urea electrosynthesis from CO_2 and NO_x^- is a complex multistep process involving multiple

[1]Particles and Catalysis Research Laboratories and School of Chemical Engineering, UNSW Sydney, Sydney, NSW 2052, Australia. [2]Center for Renewable Energy Conversion, Chemical Engineering Department, Faculty of Industrial Technology, Parahyangan Catholic University, Bandung 40141, Indonesia. [3]School of Science, Computing and Engineering Technologies, Swinburne University of Technology, Swinburne University of Technology, Melbourne, VIC 3122, Australia. [4]School of Chemical Engineering, The University of Adelaide, Adelaide, SA 5005, Australia. [5]Nanotechnology Research Laboratory, Faculty of Engineering, The University of Sydney, Sydney, NSW 2008, Australia. [6]Australian Synchrotron, ANSTO, Clayton, VIC 3168, Australia. [7]School of Chemistry, Monash University, Clayton, VIC 3800, Australia. [8]Particles and Catalysis Research Laboratories and School of Minerals and Energy Resources Engineering, UNSW Sydney, Sydney, NSW 2052, Australia. [9]Present address: Institute for Superconducting and Electronic Materials (ISEM), Australian Institute for Innovative Materials (AIIM), Innovation Campus, University of Wollongong, Wollongong, NSW 2522, Australia. ✉e-mail: thanhtran@swin.edu.au; r.daiyan@unsw.edu.au

electron transfer (Tables S1, S2, Supplementary Data 1) and competing with mechanistically simpler reduction processes, viz. the hydrogen evolution reaction (HER), CO_2 reduction reactions (CO_2RR), and NO_2^-/NO_3^- reduction reactions (NO_2^-RR/NO_3^-RR or NO_x^-RR)[2,11]. Notable challenges include limited CO_2 adsorption capacity[12], sluggish dissociation of the C=O bond[12,13], and difficulty in balancing adsorption and activation of both carbon- and nitrogen-derived species[2,14].

At the core of these challenges lies the C–N coupling step, whose mechanism remains poorly resolved due to interplay of multiple surface-bound species and dynamic changes in catalyst structure under reaction conditions. Proposed C–N coupling pathways involve intermediates such as *CO, *NO, *NH_2, and *NH, with key steps often limited by proton-coupled electron transfer (PCET) barriers[11,15–17]. Elucidating these pathways—and understanding how the catalyst surface evolves during operation—requires in situ spectroelectrochemical characterization techniques, such as Raman, infrared, and X-ray absorption spectroscopy (XAS), which can directly capture transient intermediates and structural changes[12,13]. Achieving the most energetically favorable pathway requires precise tuning of intermediate adsorption energies, a task that may be inherently challenging for a monometallic catalyst. This has led to growing interest in multimetallic designs, where distinct active sites can preferentially stabilize different intermediates and facilitate sequential steps. Indeed, such strategy has been successfully applied in the oxygen evolution reaction (OER)[18,19] and CO_2RR[20,21] fields, offering a blueprint for tackling the complexity of urea electrosynthesis.

Copper has been widely studied due to its ability to facilitate CO_2 and NO_x^- activation, moderate hydrogen binding, and tendency to form key intermediates such as *CO and *NH_2[22–27]. However, Cu suffers from limited urea selectivity and deactivation caused by strong adsorption of nitrogen intermediates[28–32]. Cobalt, on the other hand, offers high conductivity, favorable *CO binding, and the ability to stabilize *H intermediates, thereby promoting downstream protonation or hydrogenation steps[31,33–36].

These complementary characteristics led us to a working hypothesis that combining Cu and Co could couple their strengths—enhancing NO_x^- reduction to reactive nitrogen species on Cu, while stabilizing *CO and *H on Co—to accelerate C–N bond formation[31,37,38]. Supporting this concept, recent work on amorphous Cu–Co boride (a-$Cu_{0.1}CoB_x$) demonstrated alleviation of strong N-based and *CO intermediates binding on the catalyst surface and achieved a faradaic efficiency (FE) of ca 28% with a urea yield rate of ca 310 μg h^{-1} mg_{cat}^{-1} (5.2 mmol h^{-1} g_{cat}^{-1}) from CO_2 and NO_3^-[39].

In parallel, we also considered an alternative, cross-assigned tandem hypothesis—that Cu predominantly improves the CO_2 adsorption and activation, stabilizing *CO/*COOH[40,41], whereas Co primarily promotes NO_2^- activation and stabilizes N-intermediates[42,43]. To address the ambiguity and resolve the roles of the two metals, we explored tandem Cu–Co catalysts prepared via co-sputtering. This approach enables atomic-level mixing of two metals, providing different but complementary active sites for key reaction steps. We anticipated that such atomic-scale integration would enhance PCET, promote the formation of key intermediates, thereby optimizing the C–N coupling process[44–46].

To test these hypotheses, we first performed systematic electrochemical studies under varying electrolyte conditions—including pH and nitrogen-source species—to evaluate urea formation and identify optimal conditions. Guided by these results, we employed in situ spectroelectrochemical techniques—in situ Raman, synchrotron radiation Fourier-transform infrared spectroscopy (SR-FTIR), and XAS—to monitor the formation and evolution of reaction intermediates directly on the catalyst surface under operating conditions. Finally, density functional theory (DFT) calculations were performed under the optimized reaction conditions to provide atomic-scale insights into the roles of Cu and Co.

Together, these results support the alternative cross-assigned mechanism, rationalizing the observed selectivity where Cu predominantly stabilizes CO_2-derived intermediates (*CO/*COOH), and Co drives *NO_2^- reduction and stabilizing *NH_2 for C–N coupling. This integrated experimental–theoretical approach aims to unravel the C–N coupling mechanism and guide the rational design of efficient catalysts for sustainable urea electrosynthesis.

Results

Catalyst characterization

We varied Cu and Co stoichiometry within the synthesized electrodes via co-sputtering metals to form Cu_1Co_2, Cu_1Co_1, and Cu_2Co_1 onto carbon fiber paper (CFP) substrates (collectively referred to as $Cu_{(n)}Co_{(1-n)}$) and characterized as-prepared materials using a range of physiochemical characterization methods. Inductively coupled plasma mass spectrometry (ICP-MS) analysis confirmed that metals were deposited close to expected ratios (Table S3, Supplementary Data 2).

Scanning electron microscopy (SEM) coupled to energy-dispersive X-ray spectroscopic (EDS) analysis confirms uniform distribution of the Cu and Co over the surface of carbon fibers (Fig. 1a–c and Figs. S1, S2, S4). EDS analysis under low-magnification transmission electron microscopy (TEM) conditions indicates homogenous mixing of Cu and Co within the sputtered materials with no observable segregation within detection limit of individual metallic phases (Fig. 1d, e and Figs. S3–S5). Higher resolution TEM of the as-prepared catalyst indicates the presence of well-defined crystal facets of a face-centered cubic (fcc) structure with an interlayer spacing of ~1.9 and 2.1 Å. This is consistent with the fcc (200) and fcc (111) facets, respectively, of both copper and cobalt metal phases (Fig. 1f and Figs. S6)[47]. The selected area electron diffraction (SAED) patterns further validate the presence of these phases (Fig. 1g and Fig. S6). Moreover, these crystal facets remain observable even after electrochemical testing, as evidenced by the post-reaction TEM analysis (Fig. S7). X-ray diffraction (XRD) patterns of all samples exhibit a prominent peak at 43.6°, which is consistent with the (111) plane of the fcc Cu and Co metals (ICDD 00-004-0836 and 01-071-4238) (Fig. S8). A peak at 39.6° is most likely associated with the 200 signals of the monoclinic CuO phase (ICDD 01-070-6827).

X-ray photoelectron spectroscopy (XPS) was employed to elucidate the surface chemical composition of the as-prepared $Cu_{(n)}Co_{(1-n)}$ catalysts (Fig. 2a, b and Figs. S9–S14), with monometallic sputtered Cu and Co serving as references. The survey spectrum reveals distinct peaks corresponding to C 1*s*, O 1*s*, Cu 2*p* and Co 2*p*, with relative intensities of Cu 2*p* and Co 2*p* peaks following the bulk composition (Fig. S9). Fitting of the high-resolution Cu 2*p* and Co 2*p* spectra of as-synthesized catalysts using the parameters reported by Biesinger et al.[48,49] and our previous reports[50,51], as a guide displays the presence of Cu(0), Cu(I), Cu(II), Co(0), and Co(II) species, indicating oxidation of surface Cu and Co metals to Cu(I), Cu(II) and Co(II) due to air exposure (Fig. 2a, b, Figs. S11–S12, Table S4, Supplementary Data 3)[52,53]. High-resolution Cu LMM Auger spectra further confirms the presence of Cu(0), Cu(I), and Cu(II) species (Fig. S13). Analysis of the high-resolution O 1*s* spectra of $Cu_{(n)}Co_{(1-n)}$ catalysts identifies lattice (529.3 eV) and non-lattice oxygen (~531.5 and 532.5 eV) (Fig. S14)[54]. Post-reaction analysis of $Cu_{(n)}Co_{(1-n)}$ catalyst reveals changes in surface structure after 12 h electrochemical testing (vide infra) (Fig. 2a, b and Figs. S9). In addition to Cu 2*p*, Co 2*p*, C 1*s*, and O 1*s* peaks, survey spectra detect K 2*p* and K 2*s* peaks, indicating adsorption of K^+ from the electrolyte on the catalyst surface. Analysis of Co 2*p*, Cu 2*p*, and Cu LMM Auger spectra indicate further oxidation of Cu(0) and Co(0) to Cu(I), Cu(II) and Co(II) induced by the electrocatalytic testing (Figs. S11–S13)[55]. Consequently, the oxidation leads to the increased peak intensity of lattice oxygen, as seen in high-resolution O 1*s* spectra (Fig. S14). XAS measurements of $Cu_{(n)}Co_{(1-n)}$ catalysts were recorded at Cu and Co K-edges. The X-ray absorption near edge structure (XANES)

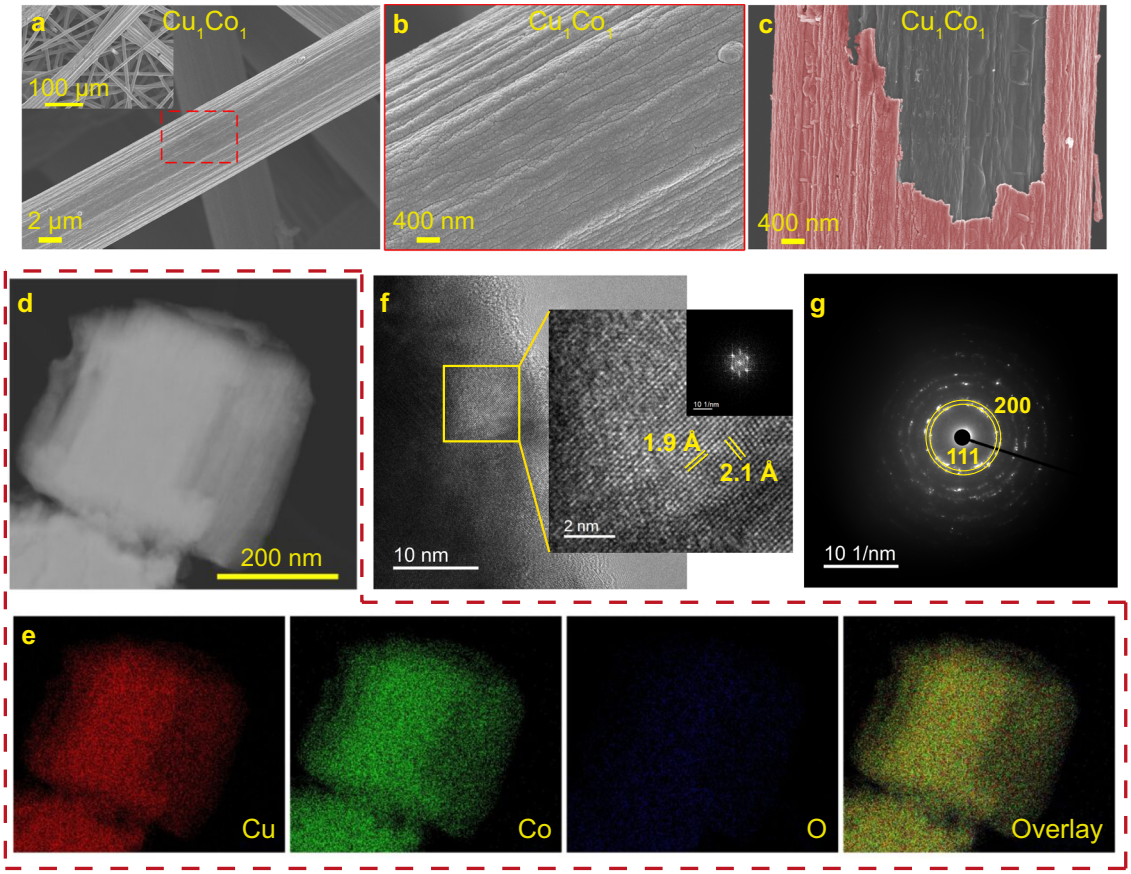

Fig. 1 | Surface morphology of the Cu_1Co_1 catalyst. a–c SEM images of an as-deposited catalyst at different magnifications; image in (**c**) is manually colorized to support the discrimination between the catalyst (red) and carbon fiber paper (gray). Scanning transmission electron microscopic (STEM) image of an as-deposited catalyst (**d**), and corresponding EDS mapping of Cu (red), Co (green), and O (blue) (**e**). **f** High resolution TEM images of an as-deposited catalyst at different magnifications. Yellow lines highlight the Cu(111) and Co(111) facets with ~2.1 Å spacing. The inset shows the corresponding fast Fourier transform (FFT) pattern (scale bar: 10 nm^{-1}), confirming the crystalline nature of the observed lattice fringes. **g** Selected area electron diffraction (SAED) pattern of an as-deposited catalyst showing diffraction ring corresponding to face-centered cubic (fcc) (111) and (200) facets.

and extended X-ray absorption fine structure (EXAFS) spectra (Fig. 2c–h and Figs. S15–S18) confirm that the as-prepared catalysts are dominated by metallic Cu(0) and Co(0), consistent with the XRD and HRTEM results. Fourier transformation (FT-EXAFS) and k^3-weighted EXAFS spectra further support this assignment (Fig. S16). Linear combination fitting (LCF) of both XANES (Figs. S19) and EXAFS (Figs. S20) indicate that the materials being composites primarily consisting of metallic Cu and Co, without evidence of intermetallic phases. In addition to the dominant metallic phases, minor Cu_2O/$Cu(OH)_2$ and Co_3O_4/$Co(OH)_2$ species are also present as detectable oxide/hydroxide phase. After electroreduction, XANES spectra (Figs. S15, S17–S18) show slight oxidation, evidenced by an increase in edge intensity, consistent with XPS results. Nevertheless, FT-EXAFS at both Cu and Co K-edges confirms that Cu–Cu and Co–Co metallic interactions remain predominant (Fig. S17–S19), with LCF analysis indicating that the post-reaction catalysts are still primarily metallic, with fractions of oxidized Cu and Co species present (Fig. S19, S20).

Raman spectroscopy was also conducted to characterize the components of the $Cu_{(n)}Co_{(1-n)}$ catalysts (Fig. S21). At 50% laser power, the as-prepared Cu_1Co_1 catalyst exhibits peaks indicative of $Co(OH)_2$ at ~530 and 600 cm^{-1}, Cu_2O at ~147 and 218 cm^{-1}, and CuO at ~294 cm^{-1} [56–60]. These oxide/hydroxide features are attributed to the oxidation of metallic Cu and Co resulting from air exposure[61,62]. Under power-dependent Raman acquisition, additional CuO and Co_3O_4 modes emerge only at higher laser power (>50%) that may indicate a laser-induced oxidation component[63,64]. Meanwhile, LCF of EXAFS spectra (Fig. S20) place an upper bound of ≤8% Co_3O_4 in $Cu_{(n)}Co_{(1-n)}$ catalysts, implying that any pre-existing Co_3O_4 is minor near-surface fraction below bulk XAS detectability. Taken together, power-dependent Raman and LCF EXAFS spectra support that the Co_3O_4 bands observed by Raman arise primarily from laser-induced oxidation, possibly superimposed on a very thin surface Co_3O_4 layer.

Comprehensive characterization confirmed that as-prepared catalysts predominantly comprise metallic Cu(0) and Co(0) states. Upon electrochemical testing, partial surface oxidations to Cu(I), Cu(II) and Co(II) were observed, with the bulk metal phases largely retained, demonstrating structural stability under reaction conditions.

Electrocatalytic performance

CO_2 and KNO_2 were selected as the carbon and nitrogen sources for our experiments to enhance C–N coupling based on our previous finding and the above discussions[65]. The Cu_1Co_1 catalyst was initially evaluated for its activity towards the CO_2RR, NO_2^-RR, and electroreduction of CO_2 and NO_2^- in the CO_2-saturated 0.2 M $KHCO_3$ solution (pH 7), Ar-saturated 0.2 M $KHCO_3$ + 0.02 M KNO_2 solution (pH 8), and CO_2-saturated 0.2 M $KHCO_3$ + 0.02 M KNO_2 solution (pH 7), respectively. To maintain saturation in these catholytes, CO_2 or Ar gas was continuously injected.

Cyclic voltammetry (CV) measurements (Fig. 3a and Figs. S22a–S25) reveal the current response of Cu_1Co_1 catalyst under each reaction condition. Notably, distinct oxidation and reduction peaks are observed between −0.1 and 0.85 V vs. RHE in all cases

https://doi.org/10.1038/s41467-026-68481-6

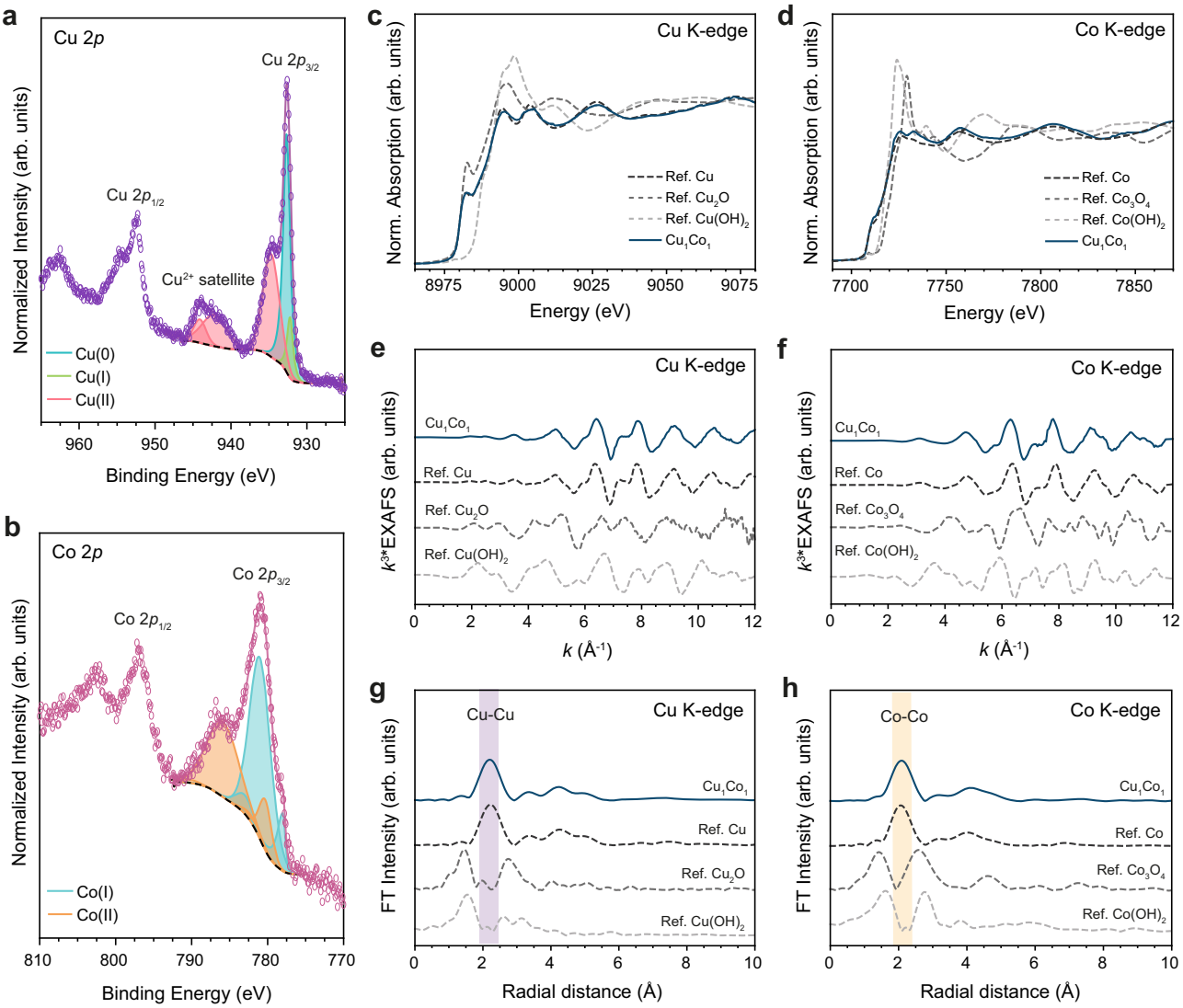

Fig. 2 | Physical characterization of the Cu_1Co_1 catalyst. High-resolution Cu 2p (**a**) and Co 2p (**b**) of as-deposited catalyst. The XANES at Cu K-edge (**c**) and Co K-edge (**d**). The k^3-weighted EXAFS spectra at Cu K-edge (**e**) and Co K-edge (**f**). The normalized FT-EXAFS of Cu_1Co_1 at Cu K-edge (**g**) and Co K-edge (**h**) of Cu_1Co_1 catalyst. In (**a**, **b**) circles denote the measured counts per second (CPS), while black dashed line represents the fitted background.

(Fig. S23), indicating the formation of Cu and Co oxides/hydroxides and their subsequent reduction. Notably, Cu_1Co_1 exhibits quasi-reversible redox behavior, in contrast to the reversible transition of pure Cu and the irreversible features of pure Co (Fig. S24)[66–69]. The irreversible nature of pure Co is likely linked to Co^{2+}/Co^{3+} dissolution into the electrolyte[70,71]. Together, these findings suggest that Cu–Co bimetallic occupy an intermediate regime, likely due to electronic and structural stabilization at the interface[72].

Furthermore, the CV profiles show that CO_2RR exhibits lower current density compared to NO_2^-RR and electroreduction of CO_2 and NO_2^-, suggesting relatively lower activity towards CO_2 reduction (Fig. 3a). Chronoamperometry (*i*-t) measurements for the CO_2RR, NO_2^-RR, and electroreduction of CO_2 and NO_2^- indicate that the Cu_1Co_1 catalyst achieves *j* of approximately −44, −80, and −64 mA cm^{-2} (−0.22, −0.41, −0.33 mA cm_{ECSA}^{-2}) at −1.2 V vs. RHE, respectively (Fig. S28-S31). NO_2^-RR testing of the Cu_1Co_1 catalyst over the potential range −0.6 to −1.2 V vs. RHE showed that the highest ammonium (NH_4^+) selectivity was achieved at −0.8 V vs. RHE with FE and yield rate of 96 ± 4% and 340 ± 9 mmol h^{-1} g_{cat}^{-1} (0.24 ± 0.006 nmol s^{-1} cm_{ECSA}^{-2}) (Fig. 3b). These values are comparable to other Cu- and Co-based catalysts in non-alkaline conditions[73,74]. CO_2RR was also conducted in the same potentials range as NO_2^-RR (Fig. 3c). At −0.6 V vs. RHE, the reaction was highly selective to formate ($HCOO^-$) with a small contribution of acetate (CH_3COO^-) and methane (CH_4). As the potential becomes more negative, the FE for formate progressively decreases while the amounts of other products, including methanol (CH_3OH^-), grows. At −1.0 V vs. RHE, the FE for CH_4, CH_3OH, and CH_3COO^- reaches 21 ± 3%, 16 ± 4%, and 12 ± 2%, respectively. The use of even more negative potential did not improve product selectivity due to the enhanced HER.

Urea electrosynthesis was conducted via co-electroreduction of CO_2 and NO_2^-. During 12 h experiments, urea was consistently detected at −1.0 V vs. RHE and more negative potentials using both ^1H NMR spectroscopy and gas chromatography with mass-spectrometry detector (GC-MS) (Fig. 3d,e and Fig. S32). Furthermore, ^{15}N isotope-tracing experiments confirm that the produced urea originates from the NO_x^- feed (Fig. S32 and Fig. S42). The highest performance was observed at −1.2 V vs. RHE, with a maximum FE of 11 ± 2% and a yield rate of 61 ± 6 mmol h^{-1} g_{cat}^{-1} (8.5 ± 0.8 nmol s^{-1} cm^{-2} per geometric surface area of the electrode or 0.043 ± 0.005 nmol s^{-1} cm_{ECSA}^{-2}).

Although CO_2RR exhibits high H_2 formation at this potential (Fig. 3c), introducing NO_2^- suppresses HER through two effects: (i)

https://doi.org/10.1038/s41467-026-68481-6

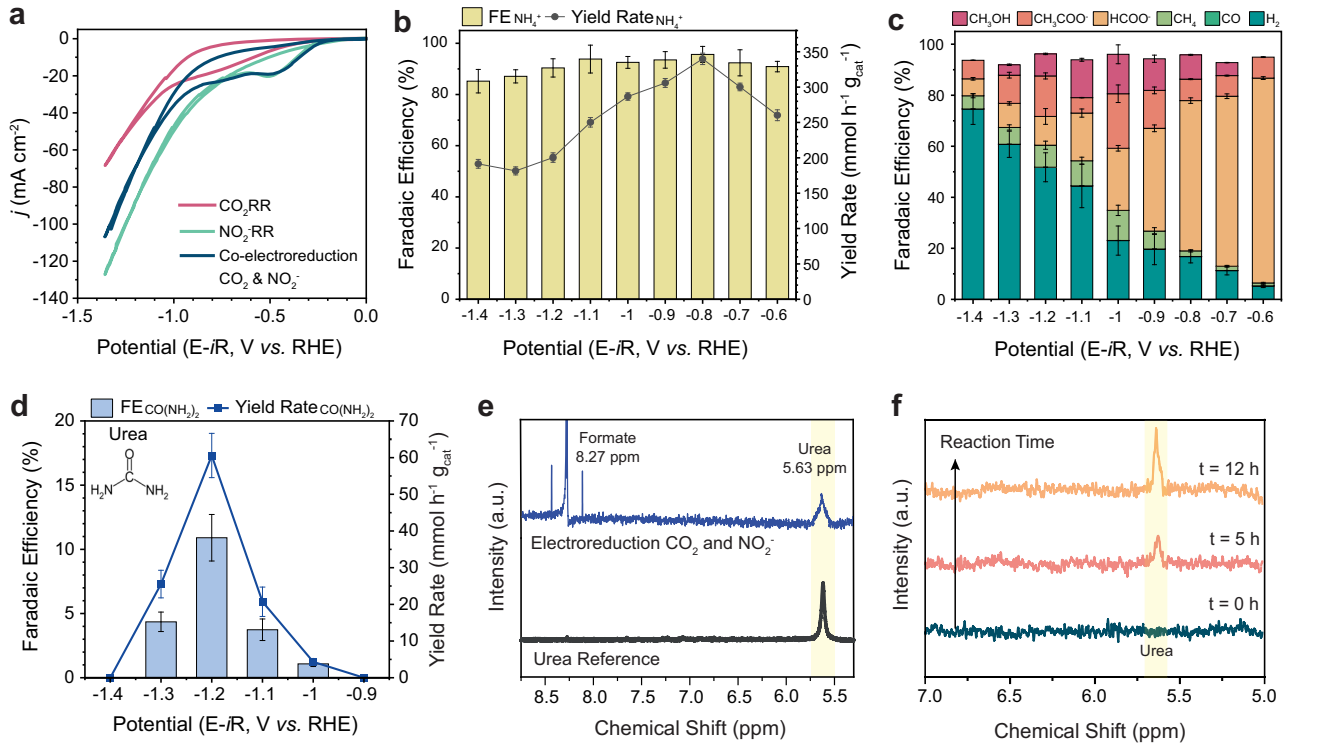

Fig. 3 | Electrochemical performance of Cu_1Co_1. **a** The cyclic voltammetry of the Cu_1Co_1 catalyst for the CO_2RR, NO_2^-RR, and electroreduction of CO_2 and NO_2^- (scan rate 20 mV s^{-1}, 5th scan shown). Currents are normalized to the geometric surface area of the electrode. **b** The FE_{NH4^+} and yield rate from the NO_2^-RR. **c** The FE of the CO_2RR products. **d** The $FE_{CO(NH2)2}$ and yield rate from the electroreduction of CO_2 and NO_2^-. **e** Representative ^{1}H NMR spectrum showing $CO(NH_2)_2$ produced at −1.2 V vs. RHE. **f** Urea detection by ^{1}H-NMR at t = 0, 5, and 12 h of the experiment at −1.2 V vs. RHE. The CO_2RR, NO_2^-RR, and electroreduction of CO_2 and NO_2^- were carried out in CO_2-saturated 0.2 M $KHCO_3$, Ar-saturated 0.2 M $KHCO_3$ and 0.02 M KNO_2, and CO_2-saturated 0.2 M $KHCO_3$ and 0.02 M KNO_2 solutions, respectively. The error bars represent the standard deviation for at least three independent measurements.

NO_2^--driven electron–proton sinking and site blocking—NO_2^- might occupy H-binding sites and lower HER[75,76]. This is consistent with the additional redox couple that appears in CV curves for Cu_1Co_1 upon NO_2^- addition (Figs. S23–S25), indicative of NO_2^--metal interaction on the catalyst surface[77]. (ii) Tandem perimeter kinetics of Cu–Co that co-generate *CO/*COOH and $*NH_2$ in close proximity (Fig. S33), as confirmed through in situ SR-FTIR (Fig. S40), thereby enabling high urea rates despite the H_2-favoring bias[75].

Time-dependent studies revealed that urea was first detectable after 5 h, with an FE and yield rate of 10 ± 1% and 56 ± 3 mmol h^{-1} g_{cat}^{-1}, respectively (Fig. 3f). The stability test further demonstrated that the Cu_1Co_1 catalyst can steadily produce urea over 48 h (Fig. S30, S31). In addition to urea, C_2 and other C–N products, such as ethanol (C_2H_5OH), acetate, and methylamine (CH_3NH_2) were detected during the experiments at −1.0 V vs. RHE, although at lower FE and yield rates (Fig. S30). The maximum FEs for methylamine, ethanol, and acetate were observed at −1.3 V vs. RHE, measuring at 1.2 ± 0.1%, 3.0 ± 0.7%, and 1.0 ± 0.1 %, respectively (Fig. S29).

When NO_3^- was used as a nitrogen source instead of NO_2^-, similar products were formed but at lower faradaic efficiencies and yield rates (Fig. 4a and Fig. S30). Urea was detected only at more negative potentials (≤−1.1 V vs. RHE) and achieved maximum values of 8 ± 1% and 26 ± 4 mmol h^{-1} g_{cat}^{-1} (0.018 ± 0.003 nmol s^{-1} cm_{ECSA}^{-2}) at −1.3 V vs. RHE (Fig. S31). This difference is consistent with our previous findings, where the activation and reduction of NO_2^- require lower overpotentials compared to NO_3^-, enabling the preferential reduction of prior reactant[65]. Supporting evidence was provided by in situ SR-FTIR spectra (Fig. S42), in which characteristic urea-related vibrations (*NCO, *CO carbonyl, and *CN) were observed more weakly in $CO_2 + NO_3^-$ than in $CO_2 + NO_2^-$ experiments[14,16,78].

To further probe nitrogen source effects, hydroxylamine (NH_2OH) was tested. Instead of urea, the reaction yielded ammonium carbamate ($[NH_4][NH_2COO]$) with FE of 16 ± 3% and yield rate of 90 ± 5 mmol h^{-1} g_{cat}^{-1} (0.064 ± 0.004 nmol s^{-1} cm_{ECSA}^{-2}) at −1.2 V vs. RHE (Fig. 4a). This suggests that the dominant process is electrochemical reduction of NH_2OH to NH_4^+, while the carbamate anion forms chemically through reaction of hydroxylamine with CO_2 [79,80]. The absence of ammonium carbamate in NO_2^- and NO_3^- experiments implies that hydroxylamine is not an intermediate in the co-reduction pathway, or if transiently formed, is rapidly converted into other species. Overall, these results establish that NO_2^- is a more effective nitrogen source than NO_3^- or NH_2OH for urea electrosynthesis. Compared with reported catalysts (Table S5, Supplementary Data 4), the Cu_1Co_1 system achieves competitive urea yield rates under prolonged operation, demonstrating its effectiveness as a tandem Cu–Co catalyst for selective C–N coupling.

We also investigated electroreduction of CO_2 and NO_2^- at −1.2 V vs. RHE using monometallic Cu and Co catalysts (Fig. S30 and Fig. S33) as control references. The sputtered Cu catalyst produced no detectable C–N products, instead yielding formate, ethanol, and propanol (Fig. S29, S47, S48). This outcome contrasts with many reports describing strong C–N coupling on Cu and underscores a more nuanced picture[15,81]. In the literature, high urea selectivity is typically associated with oxide-derived Cu, where mixed Cu(0)/Cu(I) and defect-rich surfaces stabilize polar intermediates such as *CO, *NCO and $*NH_2CO$[27,82]. By comparison, sputtered Cu typically generates thin, relatively smooth films with fewer defect sites, thereby limiting the stabilization of key intermediates required for C–N coupling[83]. Consequently, metallic Cu favors CO_2 adsorption and *CO/*COOH formation[40], consistent with the results observed in the in situ SR-FTIR spectra (Fig. S42). For pure Co, the main products were ammonium

https://doi.org/10.1038/s41467-026-68481-6

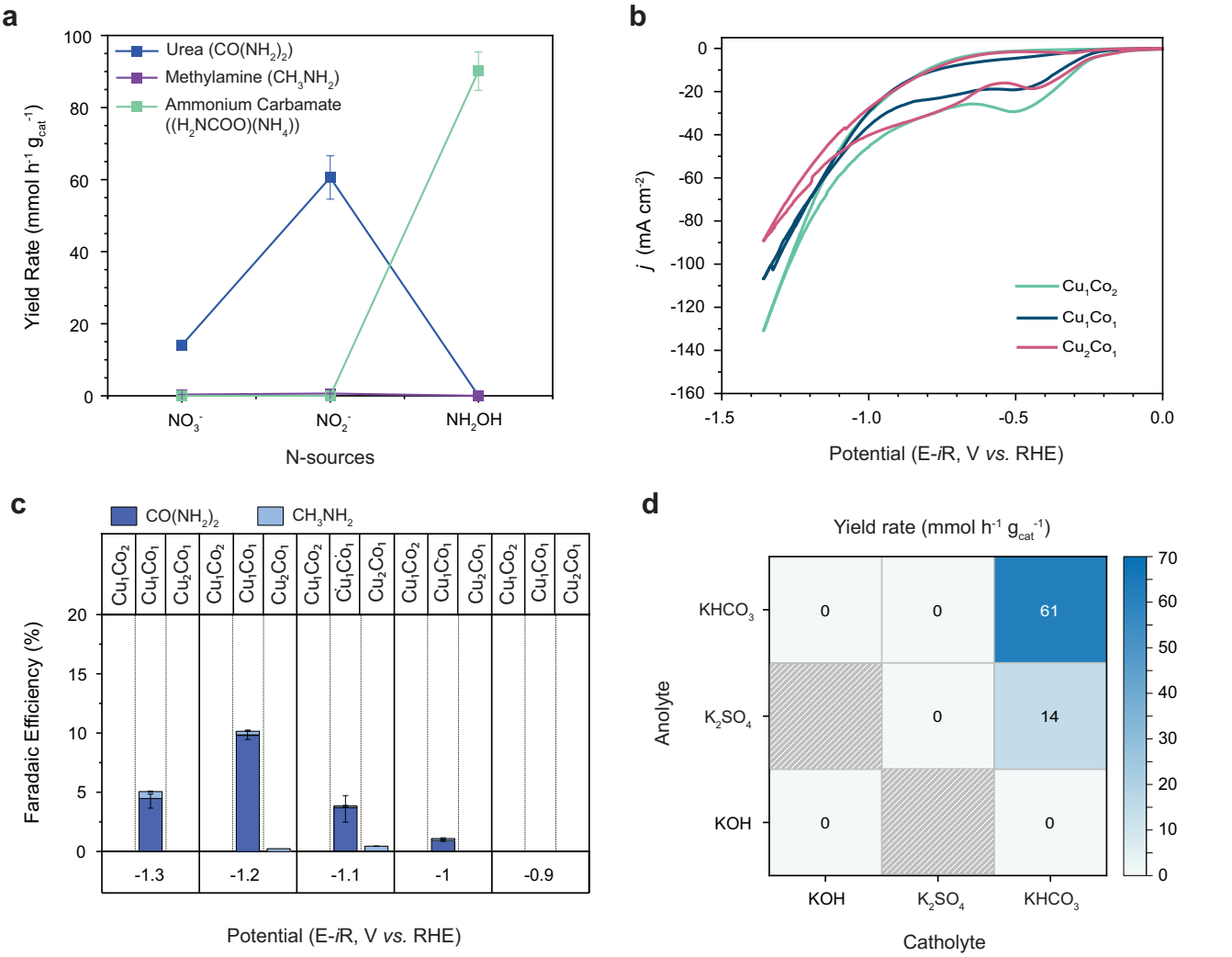

Fig. 4 | Electrochemical performance comparison of $Cu_{(n)}Co_{(1-n)}$ catalysts and effect of electrolyte. a Faradaic efficiency and yield rate of C–N products from different nitrogen sources. The concentration of nitrogen sources was kept at 0.02 M in the 0.2 M $KHCO_3$ solution. The applied potential for the test was -1.2 V vs. RHE. **b** Cyclic voltammetry curves of $Cu_{(n)}Co_{(1-n)}$ catalysts during electroreduction of CO_2 and NO_2^-. **c** Faradaic efficiency of C–N products using $Cu_{(n)}Co_{(1-n)}$ catalysts after electroreduction of CO_2 and NO_2^- for 12 h. **d** The electroreduction of CO_2 and NO_2^- in various catholyte and anolyte at −1.2 V vs. RHE. For (**a**) electroreduction of CO_2 and NO_2^- were carried out in CO_2-saturated 0.2 M $KHCO_3$ with addition of 0.02 M KNO_3 or 0.02 M KNO_2 or 0.02 M NH_2OH. Catholyte for (**b**, **c**) is CO_2-saturated 0.2 M $KHCO_3$ + 0.02 M KNO_2. The concentrations of anolyte in (**d**) are 0.1 M KOH (pH 13), 0.2 M K_2SO_4 + H_2SO_4 (pH 5), and 0.2 M $KHCO_3$ (pH 8). For catholyte in (**d**), the buffer concentrations are identical to those of the anolyte but include 0.02 M KNO_2. All testing was performed using a continues CO_2 gas flow. The error bars represent the standard deviation for at least three independent measurements.

and H_2 (Fig. S33), with no evidence of C–N products, also corroborated by in situ SR-FTIR (Fig. S42).

These controls underscore that neither Cu nor Co alone is sufficient for effective C–N coupling. Instead, the tandem interface of Cu–Co is essential: Cu sites efficiently adsorb and activate CO_2 to *CO, while Co sites accelerate the stepwise reduction of NO_2^- to $*NH_2$/$*NH_3$. The spatial co-generation and proximity of *CO and $*NH_2$ at the Cu–Co perimeter enhances the likelihood of C–N bond formation, leading to higher urea activity and selectivity than either metal alone.

Electrochemical CV measurements further highlight this synergy, as the Cu–Co bimetallic catalyst exhibits intermediate quasi-reversible behavior between pure Cu and Co (Fig. S24). This suggests that Cu suppresses Co dissolution by stabilizing its redox transitions, while Co mitigates Cu over-oxidation[78,84,85]. Such mutual stabilization likely arises from electronic and structural interactions at the Cu–Co interface, further reinforcing the unique cooperative role of the tandem system. Consistently, electrochemical impedance spectroscopy (EIS) reveals that Cu_1Co_1 has a lower charge transfer resistance compared to pure Cu and Co (Fig. S27), underscoring its enhanced electronic synergy that facilitates CO_2 and NO_2^- and underpins the C–N coupling performance of the bimetallic catalyst. This effect was not reproduced by simple physical mixing: a drop-cast Cu/Co composite produced only ammonium, formate, H_2, CO, and C_{2+} alcohols (Fig. S33), with no detectable urea. This finding demonstrates that atomic-level proximity achieved by co-sputtering is critical for cooperative interactions and the relay-type mechanism required for urea synthesis.

Given the importance of Cu and Co mixing, we also explored the effects of the Co concentration/ratio in the $Cu_{(n)}/Co_{(1-n)}$ matrix on the FE and yield rate of urea. As compared to Cu_1Co_1, the Cu_2Co_1 composition produces lower j at potentials more negative than −1.0 V vs. RHE (Fig. 4b). Methylamine is detected as the main C–N product, albeit at a low FE of less than 1%, within the potential range of −1.0 to −1.2 V vs. RHE (Fig. 4c). The increased amount of Cu in the catalyst favored the C–C coupling, producing C_{2+} products such as ethanol and n-propanol. At −1.2 V vs. RHE, the FEs for ethanol and n-propanol achieve 22 ± 4% and 2.1 ± 0.4 %, respectively. At −1.3 V vs. RHE, the FE of both products

improved to 25 ± 2% and 2.4 ± 0.7%, accordingly. Conversely, the use of the Co-rich Cu_1Co_2 catalyst enhances *j* for the electroreduction of CO_2 and NO_2^- at potentials more negative than −1.0 V vs. RHE as compared to Cu_1Co_1 (Fig. 4b). However, neither urea nor methylamine were produced. The predominant products from the Cu_1Co_2 catalyst are ammonium, formate, and H_2. These results highlight the importance of a specific Cu:Co ratio in balancing the adsorption and reduction of reactants, thus promoting urea generation without overshadowing the process with excessive side reactions (HER, CO_2RR, and NO_2^-RR). Moreover, all $Cu_{(n)}Co_{(1-n)}$ catalysts demonstrated good stability over the course of 12 h chronoamperometric experiments for the co-reduction of CO_2 and nitrite, as confirmed by ICP-MS analysis (Fig. S35), showing less than 10 wt% loss of Cu and Co. This loss is considered low compared to the literature[30,86].

Beyond tuning the Cu:Co ratio, we also explored the effects of the ion-exchange membrane and pH of the catholyte and anolyte on the effectiveness of the C–N coupling for the urea generation. Control experiments were performed by adjusting the pH of both catholyte and anolyte to acidic, neutral, and alkaline conditions under continuous CO_2-gas flow (Table S6, Supplementary Data 5). No urea was detected after co-reduction of CO_2 and NO_2^- at −1.2 V vs. RHE under either acidic (pH 3 and 5, K_2SO_4, Nafion membrane) or alkaline conditions (pH 10 and 13, KOH, anion exchange membrane (AEM)). Under alkaline conditions, formate was the dominant product, acidic electrolytes suppressed C–N coupling and steered the reaction toward H_2 and ammonium generation (Fig. S36). Urea formation was consistently observed only when $KHCO_3$ was used as buffer in both catholyte and anolyte, together with Nafion as membrane (Fig. 4d and Fig. S31). Notably, replacing Nafion membrane with AEM under identical conditions eliminated urea production (Table S6, Supplementary Data 5). These results indicate that controlled proton availability is critical for regulating surface protonation steps, consistent with a PCET pathway rather than mediation by surface-bound hydrogen (*H)[87–89]. This conclusion is further supported by in situ SR-FTIR measurements (Fig. S41), which show the absence of broad vibrational signatures characteristic of *H-related species in the 3300–3400 cm^{-1} region[90,91].

To rationalize these trends, we consider the electrolyte-dependent mechanistic factors. Neutral $KHCO_3$ maintains relatively high dissolved CO_2 concentrations, in contrast to alkaline conditions where CO_2 is converted to HCO_3^-/CO_3^{2-}, thereby enabling effective *CO/*COOH formation[92]. In acidic electrolytes, *CO can form but HER dominates surface sites and mass transport, strongly inhibiting C–N coupling[93]. For NO_2^- reduction, neutral pH provides sufficient proton activity to drive *NO hydrogenation to $*NH_2$ without excessive HER, whereas limited proton availability in alkaline electrolytes slows hydrogenation steps and reduces $*NH_2$ coverage[94–96]. Furthermore, neutral $KHCO_3$ mitigates cathodic alkalinization, stabilizing intermediates such as *NCO and $*NH_2CO$ without severe *OH blocking that occurs in strongly alkaline media[97–99].

Anolyte variation further highlighted the importance of proton flux (Table S6, Supplementary Data 5). Crucially, while the anolyte pH was varied to modulate charge transport, the catholyte bulk pH was maintained as intended, confirmed by negligible shifts (≤ ± 0.2 pH units) before and after testing. Maintaining the catholyte at neutral $KHCO_3$ but lowering the anolyte to pH 5 enabled detectable urea (FE 2 ± 0.2%, yield rate 14 ± 2 mmol h^{-1} g_{cat}^{-1}; Fig. 4F and Fig. S37), whereas excessive proton concentration (pH 3) diminished CO_2 availability and enhanced competing H_2/NH_4^+ pathways. This delicate balance in H^+ concentration reflects the interplay between CO_2 activation and NO_2^- hydrogenation, in which optimal PCET-driven protonation enables co-coverage of *CO/*COOH and $*NH_2$[23,88,100,101]. Consistent with this interpretation, in situ SR-FTIR detected their co-existence alongside urea vibrational bands under neutral conditions (Fig. S41-S42). These results indicate that urea formation depends on both an optimal Cu–Co surface and controlled proton management across both membrane and electrolyte compartments.

The role of electrolyte pH on catalyst stability is further reflected in CVs recorded in the non-catalytic potential window (Fig. S34). Acidic electrolytes promoted rapid Cu/Co redox cycling, consistent with accelerated dissolution[102,103], whereas alkaline electrolytes induced broad, hysteretic oxidation waves characteristic of irreversible oxide/hydroxide formation[99]. By contrast, neutral $KHCO_3$ displayed only weak and broadened transitions, indicating moderate surface dynamics. These CV signatures demonstrate that acidic and alkaline conditions drive aggressive redox activity and oxide formation, compromising structural integrity, whereas neutral conditions preserve a stable Cu–Co interface.

The instability was corroborated by ICP analysis of Cu and Co dissolution under strongly acidic and alkaline environments (Fig. S35). In acidic media (pH 3), Cu and Co dissolution achieved 8 ± 2 wt% and 17 ± 2 wt%, respectively. In alkaline media (pH 13), dissolution was lower (3 ± 1 wt% for Cu and 8 ± 2 wt% for Co). Such losses reduce the long-term stability and performance of the catalysts. Finally, we observed that urea is prone to decomposition into ammonium and formate/formic acid under highly acidic (pH 3, K_2SO_4) and alkaline (pH 13, KOH) conditions (Fig. S38), especially at low concentrations.

In situ spectroelectrochemical studies

To correlate surface intermediates with catalyst structure, we combined in situ Raman and SR-FTIR with XAS. In situ Raman spectroscopy (900–3400 cm^{-1}) tracked the evolution of intermediates during CO_2 and NO_2^- electroreduction (Fig. 5a and Fig. S39). Under open circuit potential (OCP), bands from bidentate nitrite (νNO_2, ~1360 cm^{-1}) and buffer solution (HCO_3^-, ~1062 cm^{-1}) were observed and persisted at −1.2 V vs. RHE[104–106]. After 20 min at −1.2 V vs. RHE, new features at ~730 (NO bending) and ~2116 cm^{-1} (CO stretching) appeared, consistent with the reduction of NO_2^- and CO_2, respectively[107–109]. Urea related vibrations at 1002 cm^{-1} (C–N) and 575 cm^{-1} (amide OCN) emerged after 30 min, but were absent in the control CO_2RR or NO_2^-RR (Fig. S38), indicating its specific association with C–N coupling[107]. Similar intermediates were identified under different applied potentials (Fig.S39), with C–N bond and OCN bending identified from −0.9 V vs. RHE. Nevertheless, the amine group intermediate signals (e.g., $*NH_2$) resulted from further reduction of NO_2^- and NO are likely undetectable in Raman spectroscopy due to weaker NH_2 vibrations and low laser power[110].

In situ SR-FTIR analysis (900–3400 cm^{-1}) provided complementary evidence of intermediate formation at various applied potentials (Fig. 5b, c). Bands assigned to $*NH_2$ bending mode (~3115 cm^{-1}), *CO stretching (~2065 cm^{-1}), $*NH_2$ rocking vibration (~1150 cm^{-1}), and $*NH_3$ rocking/wagging mode (~930 cm^{-1}) appeared from −0.8 V vs. RHE, indicative of CO_2 and NO_2^- reduction[14,82,111–113]. An amide-related *NCO vibrations (e.g., *NHCO, $*NH_2CO$, or $*NH_2COOH$), emerged around 1694 cm^{-1} from −0.9 V vs. RHE, suggesting the onset of C–N coupling formation[14,16,78]. Vibrational features assigned to the carbonyl (*CO) and *CN bonds of urea were observed at ~1590 cm^{-1} and 1455 cm^{-1}, respectively, over the potential range of −0.9 V to −1.3 V vs. RHE, align closely with the C=O and C–N stretching frequencies of the urea reference (1589 cm^{-1} and 1457 cm^{-1}, respectively; Fig. S40). In contrast, control CO_2RR and NO_2^-RR experiments display only *CO/*COOH and $*NH_2/*NH_3$ features (Fig. S41), without any C–N features, thereby indicating that *CO/*COOH and $*NH_2$ likely act as precursors for C–N coupling[14,16,17,78].

Catalyst comparison highlighted the role of the Cu–Co interface. Urea-associated carbonyl and *CN vibrational features were exclusively observed for Cu_1Co_1 (Fig. S42). Pure Cu exhibited mainly *CO (~2065 cm^{-1}) and *COOH (~ 1720 cm^{-1}) bands associated with gaseous CO and formate formation, along with a C–O stretching band (*CO) at ~1030 cm^{-1} corresponding to methanol[114]. These results indicate that

https://doi.org/10.1038/s41467-026-68481-6

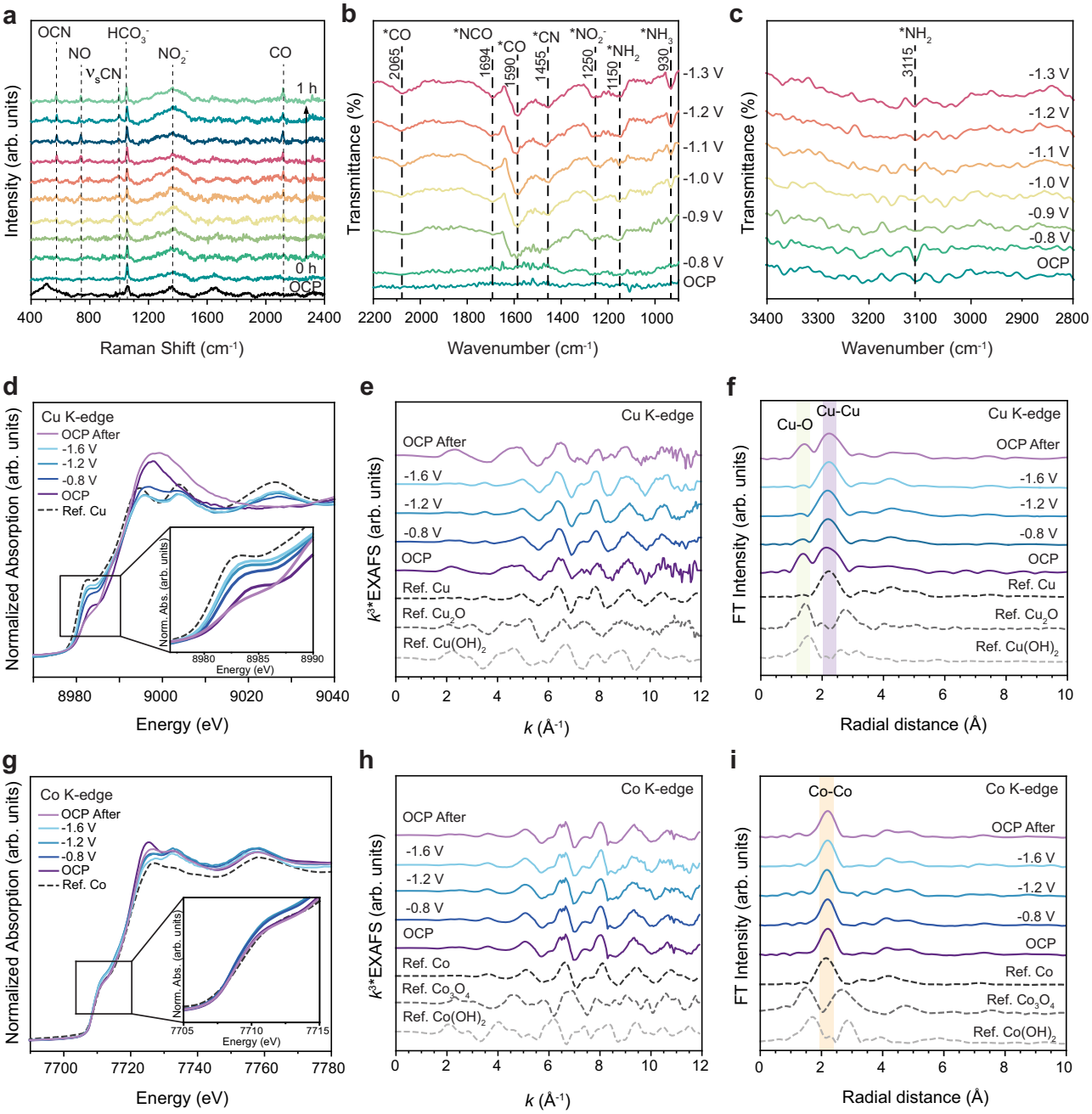

Fig. 5 | In situ spectroelectrochemical investigation of Cu_1Co_1 catalyst. (**a**) In situ Raman spectra of Cu_1Co_1 catalyst at −1.2 V vs. RHE. In situ SR-FTIR spectra of Cu_1Co_1 catalyst in the range of 900–2200 cm^{-1} (**b**) and 2800–3400 cm^{-1} (**c**). In situ XANES spectra (**d**), k^3-weighted EXAFS spectra (**e**), and FT-EXAFS spectra (**f**) of Cu_1Co_1 catalyst at Cu K-edge. In situ XANES spectra (**g**), k^3-weighted EXAFS spectra (**h**), and FT-EXAFS spectra (**i**) of Cu_1Co_1 catalyst at Co K-edge. All experiments were conducted in a CO_2-saturated 0.2 M $KHCO_3$ and 0.02 M KNO_2 solution.

CO_2RR dominates on pure Cu, consistent with earlier observations. In contrast, pure Co displayed no carbonyl or *CN bands, yielding mainly formate and ammonia. These results indicate that the Cu–Co interface promotes the C–N coupling steps leading to urea.

Isotope labeling with $^{15}NO_3^-$ confirmed the nitrogen origin of the *CN band (Fig. S43). Spectra for $^{14}NO_2^-$ and $^{14}NO_3^-$ were nearly identical, apart from an additional $*NO_3^-$ feature at ~1340 cm^{-1} [113]. Substitution with $^{15}NO_3^-$ shifted nitrogen-containing vibrational modes to lower wavenumbers, with the $*C^{15}N$ feature of urea detected at 1411 cm^{-1}, while the carbonyl peak remained unchanged[115]. This isotopic shift confirms that the *CN signal originates from NO_x^--derived nitrogen.

Catalyst structure and dynamics were probed by in situ Raman and XAS. In situ Raman spectra in the 300–1000 cm^{-1} region showed no oxides or hydroxides signals under negative potentials (Fig. S39), suggesting that the active sites during the electroreduction are in the metallic forms of Cu and Co. Only at OCP, surface hydroxides ($Co(OH)_2$ and $Cu(OH)_2$) were detected at ~502.5 cm^{-1}, implying the interaction between Cu/Co and the electrolyte[31,58,116].

The results from in situ Raman are corroborated by in situ XAS analysis at Cu and Co K-edges. The in situ XANES of Cu_1Co_1 catalyst at Cu K-edge (Fig. 5d and Fig. S44) reveals a characteristic XANES consistent with Cu(0) and a $3d^{10}$ electron configuration[25,117]. A slight shift to lower effective nuclear charge in the rising edge between 8980 and 8990 eV was observed under increasingly applied potentials, suggesting some surface copper oxides is converted to Cu(0)[118]. Additionally, the main peak (white line) during in situ conditions is shifted

to lower energies (Fig. S44), consistent with a transient reduction associated with adsorbed reactants during electrocatalytic reactions[119]. The k^3-weighted EXAFS (Fig. 5e) and normalized FT-EXAFS (Fig. 5f) at Cu K-edge confirm that the majority Cu retains characteristics of metallic Cu under negative potentials, indicating that Cu returns to its metallic state. OCP measurements before and after reaction show that Cu_1Co_1 exhibits Cu–O and Cu–Cu interactions at apparent distances of ~1.4 and ~2.2 Å, respectively. Additionally, LCF of XANES and EXAFS spectra (Fig. S49–S50) confirms that Cu(0) is the dominant component under cathodic potentials, with copper oxides and hydroxides (i.e., $Cu(OH)_2$) each accounting for <10%. These minor oxides/hydroxides species re-emerge once the potential is removed, driven by re-oxidation upon contact with the electrolyte[65,120]. Similar interaction patterns are also observed during the CO_2RR and NO_2^-RR using Cu_1Co_1 and Cu (Fig. S45-S51).

In situ XAS measurements at the Co K-edge, examining both near-edge and extended-edge structures, reveal a gradual decline in the oxidation state of the catalyst to metallic Co with increasing cathodic potential (Fig. 5g–i and Fig. S52). This change is marked by a subtle shift towards a lower effective nuclear charge between 7710 and 7718 eV, accompanied by a decrease in white-line intensity, both indicative of a reduction in the oxidation state of Co (Fig. 5g and Fig. S52). Unlike copper, which tends to form oxides under OCP condition, the k^3-weighted EXAFS (Fig. 5H) and normalized FT-EXAFS (Fig. 5i) at Co K-edge demonstrate that Co predominantly retains the properties of metallic Co under both OCP conditions and negative potentials. This is likely attributed to the dissolution of Co^{2+}/Co^{3+} species into the catholyte, rendering them undetectable by XAS. The FT-EXAFS analysis further shows a consistent increase in the intensity of Co–Co coordination at an apparent distance of 2.1 Å with the application of negative potential (Fig. S52). Comparable interaction patterns are also observed for both CO_2RR and NO_2^-RR using Cu_1Co_1 and Co (Fig. S53–S55). LCF of the XANES and EXAFS spectra further verifies that metallic Co is the principal phase under both OCP and negative potential, with trace of Co_3O_4 and $Co(OH)_2$ during cathodic potential (Fig. S56–S58).

Together, these results indicate a strong structure-activity correlation. Minor copper oxides/hydroxides detected by LCF EXAFS/XANES may, in principle, stabilize polar intermediates such as *NCO[121–123]. Similarly, cobalt oxides/hydroxides have been reported to enhance NO_2^- activation and hydrogenation[31,124]. However, these species are present only in trace amounts, and their limited surface coverage or transient lifetime appears insufficient under electroreduction conditions, as depicted in CV measurements (Fig. S23). This is consistent with the in situ SR-FTIR spectra of pure Cu, which show only weak *CN features (Fig. S42). It should also be noted that LCF provides bulk-averaged phase fractions and cannot resolve whether these minority species are surface-localized, catalytically accessible, or stable under bias; hence, their role is considered indicative rather than definitive for the active surface. Overall, the evidence indicates that Cu alone enhances CO_2 adsorption and stabilizes *CO/*COOH intermediates but lacks sufficient $*NH_2$ coverage; Co alone reduces NO_2^- to $*NH_2/*NH_3$ but provides inadequate *CO (Fig. S42). In contrast, at the Cu–Co interface, CO_2-derived *CO/*COOH from Cu and NO_2^--derived $*NH_2$ from Co are generated in close proximity, which enhances the probability of C–N bond formation. Based on these mechanistic observations, we then performed DFT modeling of the reaction pathways.

DFT calculations

Experimental results, including ex situ XAS and XPS, alongside in situ measurements of Raman and XAS, have indicated both Cu and Co metals as the dominant phases. DFT calculations are subsequently used to further understand the function of Cu and Co in the catalyst. Both Cu and Co stabilize *H intermediates on their surfaces ($\Delta G = -0.54$ and -0.62 eV) (Fig. 6a), which suppresses H_2 evolution but might not necessarily lead to significant *H-mediated hydrogenation. Rather, this stabilization maintains the catalyst surface in a state conducive to PCET, whereby proton transfer from the electrolyte, coupled with electron transfer, drives the hydrogenation of *CO/*COOH and $*NO_2^-$-derived intermediates[125]. This interpretation aligns with our experimental observations that urea formation is sensitive to proton flux across the membrane, consistent with a PCET-controlled mechanism.

DFT calculations indicate that Cu and Co exhibit distinct but complementary functions within the tandem system: (i) Cu enhances CO_2 adsorption, while Co facilitates *COOH and *CO formation during CO_2RR (Fig. 6b); and (ii) Co promotes NO_2^- adsorption, whereas Cu favors $*NH_2$ generation during NO_2^-RR (Fig. 6c and Fig. S59). This synergistic interaction aligns with in situ spectroscopic observation of *CO/*COOH and $*NH_2$ co-appearance under proton-accessible conditions. Calculations of C–N coupling pathways (Fig. 6d) further indicate that $*NH_2$ + *COOH coupling is the most thermodynamically favorable route toward urea, with the formation of $*NH_2CO$ identified as the potential-determining step ($\Delta G = 0.78$, 0.22, and 0.57 eV on Cu, Co, and Cu–Co interface, respectively; Fig. 6e). Once $*NH_2CO$ is formed, subsequent PCET steps toward $*NH_2CONH$ and $*NH_2CONH_2$ proceed spontaneously (Fig. 6f).

We acknowledge that our present models likely underestimate the contribution of defect-rich or amorphous sites, which could further lower activation barriers and stabilize key intermediates[126]. Future studies employing large-scale simulations or machine-learning-assisted approaches will be needed to better capture the structural complexity of sputtered catalysts[127]. It should also be noted that the DFT calculations are based on idealized surface models under vacuum conditions and do not fully capture solvent effects, dynamic surface reconstructions, or potential-dependent processes that occur during catalysis.

Collectively, the DFT results are qualitatively consistent with the experimental observations, suggesting that the Cu–Co interface likely balances C–N intermediate adsorption, lowers the barrier for $*NH_2CO$ formation, and facilitates proton-driven hydrogenation steps. This proposed synergy offers a plausible explanation for the experimentally observed dependence of urea formation on proton flux and electrolyte environment. Furthermore, the calculations imply that Co may mitigate the overly strong adsorption of C–N intermediates on pure Cu, while the spatial proximity of Cu and Co sites promotes the overall catalytic activity.

Discussion

In summary, we report a strategy for the electroreduction of CO_2 and NO_2^- into urea using a co-sputtered Cu_1Co_1 catalyst. This catalyst exhibits an atomic-level mixing of Cu and Co, and shows lower charge transfer resistance compared to pure Cu and Co catalysts. The Cu_1Co_1 catalyst demonstrates C–N coupling capabilities, achieving a maximum urea FE and yield rate of 11 ± 2 % and 61 ± 6 mmol h^{-1} g_{cat}^{-1} at −1.2 V vs. RHE ($j = -64$ mA cm^{-2}). The results indicate that both the Cu:Co ratio and electrolyte environment strongly influence C–N coupling. A 1:1 Cu–Co ratio provides an optimal balance between adsorption and reduction of intermediates, promoting urea formation while suppressing competing HER, CO_2RR, and NO_2^-RR. Urea formation is favored under neutral $KHCO_3$, in which proton availability is appropriately balanced to sustain PCET without diverting the pathway toward competing H_2 evolution. In situ Raman, SR-FTIR, and XAS indicate that C–N coupling proceeds through relay mechanism at the Cu–Co interface: Cu promotes CO_2 adsorption and NO_2^- activation, while Co facilitates NO_2^- adsorption and *CO/COOH formation. DFT calculations further support that urea generation arises from the coupling of $*NH_2$ and *COOH.

https://doi.org/10.1038/s41467-026-68481-6

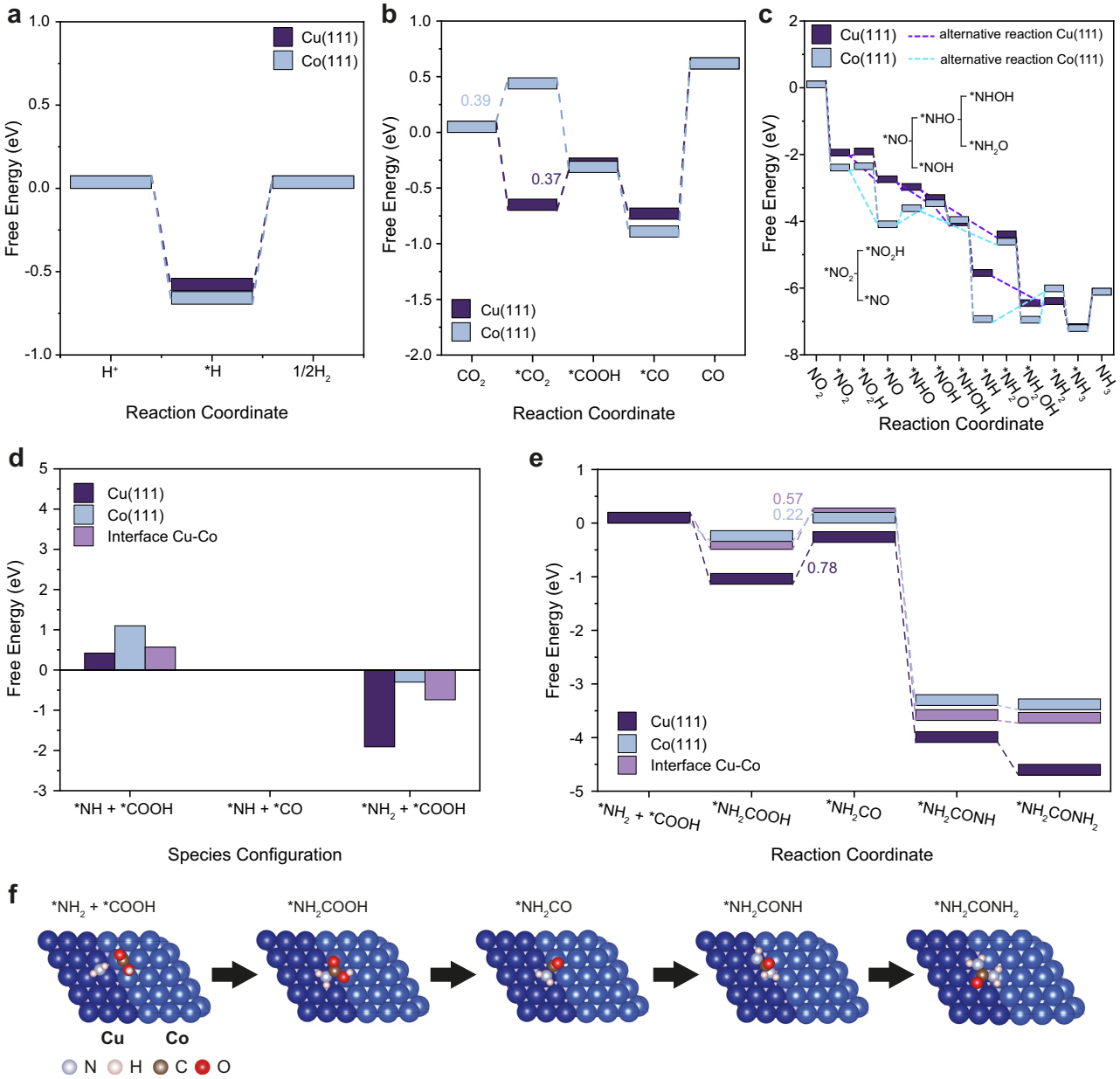

Fig. 6 | The DFT calculations for CO_2RR, NO_2^-RR, and electrochemical C–N coupling. The DFT calculations for HER (**a**), CO_2 reduction to CO (**b**), and NO_2^- reduction to NH_3 (**c**). **d** Species configuration of C–N coupling between *NH + *COOH, *NH + *CO, and $*NH_2$ + *COOH, on Cu_1Co_1 catalyst. **e** The DFT calculations of electrochemical C–N coupling. **f** Schematic illustration of Cu_1Co_1 catalyst that shows favorability of $*NH_2$ coupling with *COOH. The dash lines in (**c**) show possible DFT-calculated reaction pathways.

Methods

Materials

Catalyst precursors used to produce the co-sputtered catalyst were Cu (AJA International USA, ≥99.99%) and Co (AJA International USA, ≥99.9%). Carbon-based electrodes were using carbon fiber papers (Fuel cell store, 5% PTFE, 0.28 mm thickness, 0.44 g cm^{-3} bulk density, and 78% porosity).

Electrolyte solutions were prepared using $KHCO_3$ (Sigma-Aldrich, ≥99.7%), KNO_2 (Sigma-Aldrich, ≥99.6%), KOH (Sigma-Aldrich, ≥90%, flakes), K_2SO_4 (Sigma-Aldrich, ≥90%, powder), H_2SO_4 (Sigma-Aldrich, 95–98%) and deionized water (Satorius™ Arium®, 18.2 MΩ cm^{-1} at 23 ± 2 °C). The gases for electrochemical testing used CO_2 (Coregas, grade 2.5) and Ar (Coregas, grade 5).

Ammonium identification used Berthelot method employing NH_4Cl (Sigma-Aldrich, ≥99.99%), NaOH (Sigma-Aldrich, ≥98%), salicylic acid (Sigma-Aldrich, ≥99%), sodium citrates (Sigma-Aldrich, ≥99%), sodium hypochlorite solution (Sigma-Aldrich, 4.00–4.99%), and sodium nitroferricyanide solution (Sigma-Aldrich, ≥99%). The ^{1}H-NMR for CO_2RR liquid product and urea identification used DMSO-d_6 (Cambridge Isotope Laboratories, D-99.9%) as a solvent and sodium acetate (Sigma-Aldrich, ≥99%) as an external standard.

Identification of urea via GC-MS was employed using chemicals including acetonitrile (Sigma Aldrich, 99.8%), N-methyl-N-(t-butyldimethylsilyl)trifluoroacetamide (MtBSTFA) (Sigma Aldrich, >97%), and toluene (Sigma Aldrich, ≥99.8%). The urea identification via NMR isotope tracing was applied using $K^{15}NO3$ (Sigma Aldrich, 10 atom % ^{15}N).

Cu_2O (Sigma Aldrich, ≥99.999%, anhydrous), CuO (Sigma Aldrich, 99.99%), $Cu(OH)_2$ (Sigma Aldrich, ≥95%), CoO (Sigma Aldrich, ≥99.5%), $Co(OH)_2$ (Sigma Aldrich, ≥95%), and Co_3O_4 (Sigma Aldrich, ≥99.5%)

were applied as reference materials for XAS characterization of the catalyst.

Catalyst preparation

Cobalt and copper were deposited onto the carbon fiber paper substrate by simultaneous co-sputtering DC magnetron guns (1000 W) in 1200 s to obtain Cu–Co samples. Argon was used during the deposition in the sputter coater system (AJA Intl. – ATC-2400V). The stoichiometric ratios of Co and Cu were controlled through tuning the power of gun sources. The catalyst loading is 0.2 ± 0.02 mg cm^{-2}.

Electrochemical measurements

Electrosynthesis was performed in a three-electrode customized H-cell system using a Nafion 117 membrane to separate the compartments within a gas-tight cell. A platinum (Pt) plate and saturated calomel electrode (SCE) served as the counter and reference electrode, respectively. The reference electrode was calibrated against the reversible hydrogen electrode (RHE) in the same electrolyte prior to all measurements. The calibration was performed using a clean Pt plate as the working and counter electrodes in a H_2-saturated electrolyte. The open-circuit potential was recorded until stabilization. This calibration procedure was repeated regularly to ensure consistency across measurements. The electrolyte consisted of Ar-saturated 0.2 M $KHCO_3$, Ar-saturated 0.2 M $KHCO_3$ + 0.02 M KNO_2, and CO_2-saturated 0.2 M $KHCO_3$ were utilized as the catholyte for HER, NO_2^-RR and CO_2RR, respectively. The catholyte for C–N coupling electrosynthesis used CO_2-saturated 0.2 M $KHCO_3$ + 0.02 M KNO_2 solution. The anolyte for all electrochemical measurements used 0.2 M $KHCO_3$ solution but without gas saturation. All electrolytes were prepared freshly on the day of electrolysis to ensure solution stability and reproducibility. Before experiments, the cathodic compartment of the cell was purged with the relevant gas for 10 min, achieving pH levels of 8 ± 0.2, 7 ± 0.2, and 7 ± 0.2 for NO_2^-RR, CO_2RR and C–N coupling electrosynthesis, respectively. The Ar or CO_2 gas flowrate was maintained at 10 mL min^{-1} (9.4 standard liter per minute (SLPM)) during the HER, NO_2^-RR, CO_2RR and C–N coupling reactions. The gas flow rate was quantified using a flowmeter (Dwyer RM Rate-Master) integrated into the gas inlet line of the cell. Electrochemical testing was conducted with an Autolab M204 (Metrohm Autolab) electrochemical workstation. The tests for NO_2^-RR and CO_2RR are conducted over a duration of 1 h, while electroreduction of CO_2 and NO_2^- is carried out between 5 and 12 h. Fixed potential electrolysis was then carried out in triplicate. Following electrolysis, all potential were manually *i*R corrected, where *i* is the measured current and *R* is the electrolyte resistance (Fig. S27). The corrected potentials were then converted to the RHE reference for benchmarking with the literature using the following equation: E_{RHE} (V) = E_{SCE} (V) + 0.245 + 0.059 × pH for acidic/neutral conditions or E_{RHE} (V) = $E_{Hg/HgO}$ (V) + 0.098 + 0.059 × pH for alkaline conditions. During the adjustment of the catholyte and anolyte to acidic and alkaline conditions, as mentioned in the main text, a 0.2 M K_2SO_4 solution served as the buffer for the acidic electrolyte, with the pH being adjusted using H_2SO_4. Conversely, the alkaline electrolyte utilized a KOH solution, the concentration of which varied to achieve the desired pH levels. A Hg/HgO electrode was employed as the reference electrode in alkaline electrolytes.

The cyclic voltammetry (CV) for the electrochemically active surface area (ECSA) calculations is measured with certain potential ranges (referred to Fig. S26) at scan rate of 5, 10, 20, 40, 60, 80, and 100 mV s^{-1}. The difference between the cathodic and anodic sweeps in the CV curves plotted versus the scan rate of the CV, then fit linearly to obtain the slope that represents the double-layer capacitance (C_{dl}). The ECSA calculation follows the equation: ECSA = C_{dl}/C_s, where C_{dl} is shown in (Fig. S26), and C_s is the capacitance of an atomically planar surface (C_s is estimated to be 40 μF cm^{-2})[128,129]. The ECSA for each electrode size was then calculated by the following equation: ECSA = (cm^2_{ECSA} per $cm^2_{GEOMETRIC}$) × ($cm^2_{GEOMETRIC}$)[130]. The electrochemical impedance spectroscopy (EIS) was measured under −1.2 V vs. RHE in a CO_2-saturated 0.2 M $KHCO_3$ and 0.02 M KNO_2 solution with the frequency from 100 kHz to 0.1 Hz. The EIS fitting was conducted using The ZFit function in ECLab software version 11.42.

Product quantification

A Shimadzu gas chromatograph (Model 2010 Plus) equipped with both a thermal conductivity detector (TCD) and a flame ionization detector (FID) was employed to detect gas products such as H_2, CO, and CH_4, with calibration data provided in Fig. S60. For the quantification of liquid products from CO_2RR, ^{1}H NMR spectroscopy was used. Specifically, ~400 μL of catholyte was combined with 200 μL of DMSO-d_6 and analyzed using a 600 MHz ^{1}H 1D liquid NMR spectrometer equipped with a cryoprobe over 128 scans. An external standard method utilizing 10 mmol mL^{-1} of sodium acetate facilitated quantification.

Ammonium levels were measured using ~0.5 mL of catholyte, employing the Berthelot reaction. The reaction involved mixing the catholyte with reagent 1 (comprising 0.4 mL of 1 M sodium hydroxide, 5 wt% salicylic acid, and 5 wt% sodium citrates). This mixture was then combined with 0.1 mL of reagent 2 (0.05 M sodium hypochlorite solution) and 30 μL of reagent 3 (1 wt% sodium nitroferricyanide solution). Following sonication and a 2-h incubation in the dark at room temperature, the ammonium concentration was quantified using a Shimadzu UV-3600 UV-vis-NIR spectrophotometer and 1 cm quartz cuvettes, measuring absorbance between 550 and 800 nm wavelengths. Calibration curve data (Fig. S61) from electrolyte solutions with known NH_4Cl concentrations were used for this purpose.

Furthermore, identification and quantification of urea and other liquid products in C–N coupling electrosynthesis were performed using the ^{1}H NMR method as described by Huang et al.[131]. Approximately 400 μL of liquid sample was mixed with 200 μL of DMSO-d_6 solution (D-99.9%, Cambridge Isotope Laboratories) and analyzed in a 600 MHz ^{1}H 1D liquid NMR spectrometer (Bruker Advance) equipped with a cryoprobe over 512 scans[131]. The ^{1}H spectrum was recorded using the water suppression excitation sculpting technique, and quantification of urea was determined using the calibration curve of various urea concentration detected in the ^{1}H-NMR method (Fig. S61). For isotope tracing of urea using the ^{1}H NMR method, K^{15}NO3 was employed as nitrogen sources.

Other than NMR technique, GC-MS is also used to identify urea. Approximately 100 μL liquid sample was dried using nitrogen evaporator needle system (~10 min per 50 μL). After drying, sample was derivatized to its t-butyldimethylsilyl ester form at 60 °C for 1 h by adding 10 μL acetonitrile and 40 μL N-methyl-N-(t-butyldimethylsilyl) trifluoroacetamide (MtBSTFA) that consisted of 1% t-butyldimethylchlorosilane (tBDMCS). Derivatives were reconstituted in 40 μL toluene, then injected (1 μL splitless = 0.25–1.25 μL media equivalent on column) into GC-MS for analysis. If sample consists of urea, it will contain urea derivatives, Urea, N, N′-bis(tert-butyldimethylsilyl).

The faradaic efficiency (FE) and yield rate of liquid products were calculated to evaluate the catalytic performance using the following equations:

$$FE(\%) = \frac{n \times F \times V_{aq} \times C_{\text{Product}}}{Q} \times 100\% \quad (1)$$

where n is number of electron transfers, F is the Faraday constant (96485.33 C mol^{-1}), V_{aq} is the volume of catholyte solution (L), C_{Product} is the concentration of product (M), and Q is passed charge (C).

$$Yield\ rate_{\text{Product}}(mmol h^{-1} g_{cat}^{-1}) = \frac{C_{\text{Product}} \times V_{aq} \times MW}{t \times A \times \Gamma} \quad (2)$$

where MW is the molecular weight of product, t is duration of the electrolysis (h), A is the geometric surface area of the electrode (cm^2), and Γ is the catalyst loading per geometric surface area of the electrode (g cm^{-2}); $C_{Product}$ for this calculation is expressed in mM.

The faradaic efficiency of the gaseous products was calculated using the following equation:

$$FE(\%) = \frac{n \times F \times V_{gas} \times x}{Q} \times 100\% \quad (3)$$

where V_{gas} is the volume of headspace (L), and x is the concentration of the product in the headspace (mol L_{gas}^{-1}).

Material characterization

XRD patterns were obtained using a D2 Phaser Bruker instrument equipped with Cu Kα radiation (λ = 1.54 Å) across a scan range of 10° to 80° at a rate of 1.17 degrees per minute. The catalyst on CFP was positioned on a zero-diffraction plate made of silicon crystal. XPS was performed using a Thermo ESCALAB250Xi spectrometer, utilizing a monochromated Al Kα source (energy 1486.68 eV), operated at 120 W (13.8 kV × 8.7 mA), with a hemispherical analyzer in fixed analyzer transmission mode. The vacuum chamber maintained a pressure typically between 10^{-9} and 10^{-8} mbar. Survey spectra were recorded at a pass energy of 100 eV, and high-resolution spectra for individual peaks were acquired at 20 eV pass energy. The photoelectron take-off angle was set at 90°, with a spot size of ~500 μm. Data analysis was facilitated using ThermoScientific Avantage software. Elemental identification and quantification were achieved through survey spectra, with atomic concentrations determined using integral peak intensities and sensitivity factors provided by the manufacturer. Binding energies were calibrated to the C 1*s* peak at 284.8 eV, representing aliphatic hydrocarbons. The accuracy of quantitative XPS is estimated at 10–15%, with a precision often exceeding 5%. The peak in the XPS spectrum was deconvoluted using the CasaXPS software.

Morphological analysis was performed using a Zeiss Ultraplus field-emission scanning electron microscope (FESEM) operating at 3 kV and a JEOL 2100F high-resolution TEM at 200 kV. For SEM, electrode samples were mounted on specimen stubs using carbon tape. TEM samples were prepared by scraping material off the electrode surface and dispersing it onto holey carbon-coated nickel grids. Elemental mapping was conducted using a JEOL SDD energy-dispersive X-ray spectrometer coupled with the JEOL 2100F. The HRTEM and SAED analysis were performed with a JEOL JEM-F200. Sample was place on in-situ holders. This instrument achieves a lattice resolution of 0.16 nm in annular dark-field scanning STEM (ADF-STEM) mode and 0.1 nm in TEM mode at 200 kV. Additionally, the F200 features a JEOL 100 mm^2 energy-dispersive X-ray (EDX) detector that offers an energy resolution of 130 eV (Mn K) and a collection angle of 0.9 steradian. Ex situ Raman measurements were performed using an inVia Raman spectrometer (Horiba JOBIN YVON US/HR800 UV) with a 633 nm laser wavelength. X-ray absorption spectroscopy (XAS) of the Cu K-edge and Co K-edge was carried out at the Australian Synchrotron (ANSTO), in the XAS and Medium Energy X-ray Absorption (MEX-1) spectroscopy beamlines. Fluorescence detection was used for powder data, with Cu foil, Cu_2O, $Cu(OH)_2$, CuO, Co foil, CoO, $Co(OH)_2$ and Co_3O_4 serving as reference samples. XAS data were analyzed using Athena software and the fitting using linear combination function. MS Excel and Origin were used for the final presentations of data and fine calibrations.

For post-reaction characterization, the catalysts were subjected to 12 h of electroreduction in CO_2-saturated 0.2 M $KHCO_3$ + 0.02 M KNO_2 solution. After electrolysis, the samples were collected, rinsed with deionized water, and stored in a vacuum chamber until further analysis.

In situ measurements

In situ SR-FTIR measurements were conducted at the Australian Synchrotron (ANSTO), Melbourne using an SR-FTIR setup that incorporated a ZnSe crystal as the infrared transmission window (cut-off energy 625 cm^{-1}). This setup was paired with an infrared microscope (Bruker Hyperion 3000 with a 20x objective) and an FTIR spectrometer (Bruker 70 v/s) featuring a KBr beam splitter and a liquid-nitrogen-cooled mercury cadmium telluride detector. The catalyst electrode was positioned closely against the ZnSe crystal window with a micrometer-scale gap to reduce infrared light loss. The system was operated in reflection mode with vertical infrared light incidence to maintain the integrity of the SR-FTIR spectra. Each infrared absorption spectrum was derived by averaging 256 scans at a resolution of 2 cm^{-1}. Before conducting systematic measurements, a background spectrum of the catalyst electrode was recorded at open-circuit voltage. The potential settings for the electroreduction reaction were established at −0.8, −0.9, −1.0, −1.1, −1.2, and −1.3 V vs. RHE using CO_2-saturated 0.2 M $KHCO_3$ and 0.02 M KNO_2 as catholyte. Fig. S62 illustrates the in situ electrochemical cell and setup configuration.

In situ Raman measurements were carried out using an inVia Raman spectrometer system (Horiba JOBIN YVON US/HR800 UV) with a spectro-electrochemical Raman cell. The Raman cell was operated using a 633 nm argon ion laser and was equipped with an Ag/AgCl reference electrode and a Pt wire counter electrode. The cell contained an electrolyte solution of CO_2-saturated 0.2 M $KHCO_3$ + 0.02 M KNO_2 and was connected to an Autolab potentiostat (PGSTAT204) for simulating electrocatalytic C–N coupling.

In situ XAS measurements was carried out based on previous experiment[132]. In situ Cu K-edge and Co K-edge XAS data were gathered on the multipole wiggler XAS beamline (12-ID) at the ANSTO, Melbourne. The beamline operated with an electron beam energy of 3.0 GeV and a beam current of 200 mA (top-up mode), using “mode 1” and “mode 2” for Co K-edge and Cu K-edge, respectively, with a Si(111) monochromator and focusing optics, achieving a beam flux of ~2×10^{11} photons per second and a beam size of 0.5 mm × 0.3 mm. Data collection was conducted in fluorescence mode with a solid-state 18-element detector. The in situ cell (Fig. S63) was mounted on the beamline sample table, positioning the electrode at a 45° angle to the fluorescence detector. An OKEN ionization chamber measured the incident radiation, and all measurements were taken at ambient temperature (23 ± 1 °C).

To minimize air absorption of fluorescent X-rays, the sample environment was maintained in a helium atmosphere by connecting a flight tube between the beamline and the cell and applying a helium overpressure between the cell and detector. Each X-ray absorption near edge structure (XANES) and extended X-ray absorption fine structure (EXAFS, k = 12) spectrum required ~15 and 30 min, respectively. Data was collected at multiple sample spots to confirm homogeneity. The raw data was processed in Athena.

DFT calculations

First-principles density functional theory (DFT) calculations were performed using the Vienna Ab initio Simulation Package (VASP)[133,134]. The electronic wave functions were treated using the Projector Augmented Wave (PAW) approach[135,136]. The exchange correlation functionals were approximated by the generalized gradient approximation (GGA) as parameterized by the Perdew-Burke-Ernzerhof (PBE)[137]. The plane-wave cut-off energy of 500 eV and 3 × 3 × 1 Gamma k-point were used for the electronic self-consistent calculation, until it was converged to 1×10^{-5} eV. The ionic relaxation steps were performed using the conjugate-gradient method (IBRION = 2) and continued until the total force on each atom dropped below a tolerance of −0.05 eV/Å.

Surface investigations were studied using slab methods, for the hybrid Co (111) and Cu (111) surfaces. A vacuum region with the thickness of 20 Å was introduced perpendicular to the surface

(in the z-direction). To model the bulk-surface interface, atoms in the two outermost layers were allowed to relax, while the coordinates of atoms in other layers were fixed to their bulk positions. The free energy diagrams were developed by taking into accounts the zero-point energy and entropy contributions. Additionally, long-range van der Waals interactions were considered using DFT D-3 method[138].

Data availability

All data supporting this study are available within the article and the Supplementary Information. Source and supplementary data are provided with this paper. All other relevant source data is available from the corresponding authors upon request. Source data are provided with this paper.

References

1. Fortune Business Insight. *Urea Market Size, Share & Industry Analysis*, https://www.fortunebusinessinsights.com/urea-market-106850 (2024).
2. Yuan, J. et al. Photo/electrochemical urea synthesis via CO_2 coupling with nitrogenous small molecules: Status and challenges for the development of mechanism and catalysts. *Appl. Catal. B Environ.* **339**, 123146 (2023).
3. Mao, C., Byun, J., MacLeod, H. W., Maravelias, C. T. & Ozin, G. A. Green urea production for sustainable agriculture. *Joule* **8**, 1224–1238 (2024).
4. Cho, H. H., Strezov, V. & Evans, T. J. Environmental impact assessment of hydrogen production via steam methane reforming based on emissions data. *Energy Rep.* **8**, 13585–13595 (2022).
5. John, J., MacFarlane, D. R. & Simonov, A. N. The why and how of NO_x electroreduction to ammonia. *Nat. Catal.* **6**, 1125–1130 (2023).
6. Winter, L. R. & Chen, J. G. N_2 fixation by plasma-activated processes. *Joule* **5**, 300–315 (2021).
7. Sun, J. et al. A hybrid plasma electrocatalytic process for sustainable ammonia production. *Energ. Environ. Sci.* **14**, 865–872 (2021).
8. Miao, R. et al. Recent advances in electrocatalytic upgrading of nitric oxide and beyond. *Appl. Catal. B Environ.* **344**, 123662 (2024).
9. Barbagli, T., van Ruijven, J., Voogt, W. & van Winkel, A. *Soilless USDA-Organic Cultivation of Tomato with 'Natural Nitrogen'* 1–28 (Wageningen University & Research, 2022).
10. Williamson, R. *Australian Start-up Targets Fertiliser and Hydrogen Markets with Plasma-to-Ammonia Tech*, https://reneweconomy.com.au/australian-start-up-targets-fertiliser-and-hydrogen-markets-with-plasma-to-ammonia-tech (2023).
11. Liu, J., Guo, X., Frauenheim, T., Gu, Y. & Kou, L. Urea electrosynthesis accelerated by theoretical simulations. *Adv. Funct. Mater.* **34**, 2313420 (2023).
12. Yuan, M. L. et al. Unveiling electrochemical urea synthesis by co-activation of CO_2 and N_2 with Mott-Schottky heterostructure catalysts. *Angew. Chem. Int Ed.* **60**, 10910–10918 (2021).
13. Yuan, M. L. et al. Electrochemical C-N coupling with perovskite hybrids toward efficient urea synthesis. *Chem. Sci.* **12**, 6048–6058 (2021).
14. Zhang, X. R. et al. Identifying and tailoring C-N coupling site for efficient urea synthesis over diatomic Fe-Ni catalyst. *Nat. Commun.* **13**, 5337 (2022).
15. Lv, C. D. et al. Selective electrocatalytic synthesis of urea with nitrate and carbon dioxide. *Nat. Sustain* **4**, 868–876 (2021).
16. Luo, Y. et al. Selective electrochemical synthesis of urea from nitrate and CO_2 via relay catalysis on hybrid catalysts. *Nat. Catal.* **6**, 939–948 (2023).
17. Meng, N. N., Huang, Y. M., Liu, Y., Yu, Y. F. & Zhang, B. Electrosynthesis of urea from nitrite and CO_2 over oxygen vacancy-rich ZnO porous nanosheets. *Cell Rep. Phys. Sci.* **2**, 5452 (2021).
18. Chen, J. Y. et al. Dual single-atomic Ni-N_4 and Fe-N_4 sites constructing Janus hollow graphene for selective oxygen electrocatalysis. *Adv. Mater.* **32**, 2003134 (2020).
19. Zhu, J. Y. et al. Iridium nanotubes as bifunctional electrocatalysts for oxygen evolution and nitrate reduction reactions. *ACS Appl. Mater. Inter.* **12**, 14064–14070 (2020).
20. Wu, Z., Wu, Z., Zhao, Y. & Hou, L. Copper/Cobalt-loaded carbon nanostructures as catalysts for electrochemical CO_2 reduction. *ACS Appl. Nano Mater.* **7**, 10479–10489 (2024).
21. Hu, C. et al. Selective CO_2 reduction to CH_3OH over atomic dual-metal sites embedded in a metal-organic framework with high-energy radiation. *Nat. Commun.* **14**, 4767 (2023).
22. Zhang, H., Gao, J., Raciti, D. & Hall, A. S. Promoting Cu-catalysed CO_2 electroreduction to multicarbon products by tuning the activity of H_2O. *Nat. Catal.* **6**, 807–817 (2023).
23. Xie, Y. et al. High carbon utilization in CO_2 reduction to multi-carbon products in acidic media. *Nat. Catal.* **5**, 564–570 (2022).
24. Liu, S. L. et al. AuCu nanofibers for electrosynthesis of urea from carbon dioxide and nitrite. *Cell Rep. Phys. Sci.* **3**, 100869 (2022).
25. Leverett, J. et al. Tuning the coordination structure of Cu-N-C single atom catalysts for simultaneous electrochemical reduction of CO_2 and NO_3^- to urea. *Adv. Energy Mater.* **12**, 2201500 (2022).
26. Fu, S. et al. Ultrasonic-assisted hydrothermal synthesis of RhCu alloy nanospheres for electrocatalytic urea production. *Chem. Commun.* **59**, 4344–4347 (2023).
27. Dai, Z. et al. Surface engineering on bulk Cu_2O for efficient electrosynthesis of urea. *Nat. Commun.* **16**, 3271 (2025).
28. Jouny, M. et al. Formation of carbon–nitrogen bonds in carbon monoxide electrolysis. *Nat. Chem.* **11**, 846–851 (2019).
29. Li, J. & Kornienko, N. Electrochemically driven C–N bond formation from CO_2 and ammonia at the triple-phase boundary. *Chem. Sci.* **13**, 3957–3964 (2022).
30. Speck, F. D. & Cherevko, S. Electrochemical copper dissolution: a benchmark for stable CO_2 reduction on copper electrocatalysts. *Electrochem. Commun.* **115**, 106739 (2020).
31. He, W. et al. Splicing the active phases of copper/cobalt-based catalysts achieves high-rate tandem electroreduction of nitrate to ammonia. *Nat. Commun.* **13**, 1129 (2022).
32. Wang, Y., Zhou, W., Jia, R., Yu, Y. & Zhang, B. Unveiling the activity origin of a copper-based electrocatalyst for selective nitrate reduction to ammonia. *Angew. Chem. Int. Ed.* **59**, 5350–5354 (2020).
33. Gao, S. et al. Partially oxidized atomic cobalt layers for carbon dioxide electroreduction to liquid fuel. *Nature* **529**, 68–71 (2016).
34. Sun, Y. et al. Atomically-thin non-layered cobalt oxide porous sheets for highly efficient oxygen-evolving electrocatalysts. *Chem. Sci.* **5**, 3976–3982 (2014).
35. He, C. et al. Bimetallic cobalt–copper nanoparticle-decorated hollow carbon nanofibers for efficient CO_2 electroreduction. *Front. Chem.* **10**, 904241 (2022).
36. Guo, Y., Stroka, J. R., Kandemir, B., Dickerson, C. E. & Bren, K. L. Cobalt metallopeptide electrocatalyst for the selective reduction of nitrite to ammonium. *J. Am. Chem. Soc.* **140**, 16888–16892 (2018).
37. Azuma, M., Hashimoto, K., Hiramoto, M., Watanabe, M. & Sakata, T. Electrochemical reduction of carbon dioxide on various metal electrodes in low-temperature aqueous $KHCO_3$ media. *J. Electrochem Soc.* **137**, 1772–1778 (1990).
38. Feaster, J. T. et al. Understanding selectivity for the electrochemical reduction of carbon dioxide to formic acid and carbon monoxide on metal electrodes. *ACS Catal.* **7**, 4822–4827 (2017).
39. Wu, Y. et al. Trace Cu-induced low C—N coupling barrier on amorphous co metallene boride for boosting electrochemical urea production. *Small* **20**, 2407679 (2024).

40. Wang, L. et al. Electrochemical carbon monoxide reduction on polycrystalline copper: Effects of potential, pressure, and pH on selectivity toward multicarbon and oxygenated products. *ACS Catal.* **8**, 7445–7454 (2018).
41. Garza, A. J., Bell, A. T. & Head-Gordon, M. Mechanism of CO_2 reduction at copper surfaces: Pathways to C_2 products. *ACS Catal.* **8**, 1490–1499 (2018).
42. Niu, S. et al. Cobalt-oxygen coordination steering *NO Hydrogenation in nitrate electroreduction. *Angew. Chem. Int. Ed.* **64**, e202508227 (2025).
43. Yang, B. et al. Electron-deficient cobalt nanocrystals for promoted nitrate electrocatalytic reduction to synthesize ammonia. *Nano Energy* **117**, 108901 (2023).
44. Liu, W. et al. Electrochemical CO_2 reduction to ethylene by ultrathin CuO nanoplate arrays. *Nat. Commun.* **13**, 1877 (2022).
45. Chen, Y. et al. Efficient multicarbon formation in acidic CO2 reduction via tandem electrocatalysis. *Nat. Nanotechnol.* **19**, 311–318 (2023).
46. Sun, H. et al. Atomically dispersed Co–Cu alloy reconstructed from metal-organic framework to promote electrochemical CO_2 methanation. *Nano Res.* **16**, 3680–3686 (2022).
47. Xiao, L. et al. Identification of Cu(111) as superior active sites for electrocatalytic NO reduction to NH_3 with high single-pass conversion efficiency. *Angew. Chem. Int. Ed.* **63**, e202319135 (2024).
48. Biesinger, M. C., Lau, L. W. M., Gerson, A. R. & Smart, R. S. C. Resolving surface chemical states in XPS analysis of first row transition metals, oxides and hydroxides: Sc, Ti, V, Cu and Zn. *Appl. Surf. Sci.* **257**, 887–898 (2010).
49. Biesinger, M. C. et al. Resolving surface chemical states in XPS analysis of first row transition metals, oxides and hydroxides: Cr, Mn, Fe, Co and Ni. *Appl. Surf. Sci.* **257**, 2717–2730 (2011).
50. Tran-Phu, T. et al. Understanding the activity and stability of flame-made Co_3O_4 spinels: A route towards the scalable production of highly performing OER electrocatalysts. *Chem. Eng. J.* **429**, 132180 (2022).
51. Tran-Phu, T. et al. Understanding the role of (W, Mo, Sb) dopants in the catalyst evolution and activity enhancement of Co_3O_4 during water electrolysis via in situ spectroelectrochemical techniques. *Small* **19**, 2208074 (2023).
52. Chung, K. et al. Non-oxidized bare copper nanoparticles with surface excess electrons in air. *Nat. Nanotechnol.* **17**, 285–291 (2022).
53. Jiang, S., D'Amario, L. & Dau, H. Copper carbonate hydroxide as precursor of interfacial CO in CO_2 electroreduction. *Chemsuschem* **15**, e202102506 (2022).
54. Idriss, H. On the wrong assignment of the XPS O1s signal at 531–532 eV attributed to oxygen vacancies in photo- and electrocatalysts for water splitting and other materials applications. *Surf. Sci.* **712**, 121894 (2021).
55. Joo, J. et al. Mn-Dopant differentiating the Ru and Ir oxidation states in catalytic oxides toward durable oxygen evolution reaction in acidic electrolyte. *Small Methods* **6**, 2101236 (2021).
56. Ravindra, A. V., Behera, B. C. & Padhan, P. Laser induced structural phase transformation of cobalt oxides nanostructures. *J. Nanosci. Nanotechnol.* **14**, 5591–5595 (2014).
57. Guo, S.-X. et al. Facile electrochemical co-deposition of a graphene–cobalt nanocomposite for highly efficient water oxidation in alkaline media: direct detection of underlying electron transfer reactions under catalytic turnover conditions. *Phys. Chem. Chem. Phys.* **16**, 19035–19045 (2014).
58. Lei, Q. et al. Structural evolution and strain generation of derived-Cu catalysts during CO_2 electroreduction. *Nat. Commun.* **13**, 4857 (2022).
59. Yang, J., Liu, H., Martens, W. N. & Frost, R. L. Synthesis and characterization of cobalt hydroxide, cobalt oxyhydroxide, and cobalt oxide nanodiscs. *J. Phys. Chem. C.* **114**, 111–119 (2009).
60. Sayeed, M. A., Herd, T. & O'Mullane, A. P. Direct electrochemical formation of nanostructured amorphous $Co(OH)_2$ on gold electrodes with enhanced activity for the oxygen evolution reaction. *J. Mater. Chem. A* **4**, 991–999 (2016).
61. Tompkins, H. G. & Augis, J. A. The oxidation of cobalt in air from room temperature to 467 °C. *Oxid. Met.* **16**, 355–369 (1981).
62. Abd-El-Nabey, B. A., El-Housseiny, S., Abdel-Gaber, A. M. & Mohamed, M. E. Kinetics of oxidation of metals in the air at room temperature using EDX. *Results Chem.* **5**, 100876 (2023).
63. Speer, S. et al. Laser induced oxidation Raman spectroscopy as an analysis tool for iridium-based oxygen evolution catalysts. *Phys. Chem. Chem. Phys.* **27**, 2570–2577 (2025).
64. Rivas-Murias, B. & Salgueiriño, V. Thermodynamic CoO–Co_3O_4 crossover using Raman spectroscopy in magnetic octahedron-shaped nanocrystals. *J. Raman Spectrosc.* **48**, 837–841 (2017).
65. Ramadhany, P. et al. Triggering C–N coupling on metal oxide nanocomposite for the electrochemical reduction of CO_2 and NO_x^- to formamide. *Adv. Energy Mater.* **14**, 2401786 (2024).
66. Caballero-Briones, F., Artés, J. M., Díez-Pérez, I., Gorostiza, P. & Sanz, F. Direct observation of the valence band edge by in situ ECSTM-ECTS in p-type Cu_2O layers prepared by copper anodization. *J. Phys. Chem. C.* **113**, 1028–1036 (2008).
67. Gong, Q., Sun, L.-P., Wu, Z., Huo, L.-H. & Zhao, H. Enhanced non-enzymatic glucose sensing of Cu–BTC-derived porous copper@carbon agglomerate. *J. Mater. Sci.* **53**, 7305–7315 (2018).
68. Dong, S., Xie, Y. & Cheng, G. Cyclic voltammetric and spectroelectrochemical studies of copper in alkaline solution. *Electrochim. Acta* **37**, 17–22 (1992).
69. Ren, S. et al. Facile synthesis of petal-like nanocrystalline Co_3O_4 film using direct high-temperature oxidation. *J. Mater. Sci.* **54**, 7922–7930 (2019).
70. Schubert, N., Schneider, M. & Michealis, A. The mechanism of anodic dissolution of cobalt in neutral and alkaline electrolyte at high current density. *Electrochim. Acta* **113**, 748–754 (2013).
71. Priamushko, T. et al. Be aware of transient dissolution processes in Co_3O_4 acidic oxygen evolution reaction electrocatalysts. *J. Am. Chem. Soc.* **147**, 3517–3528 (2025).
72. Li, M. et al. Stabilizing Cu-based catalyst for electrochemical CO_2 reduction using incorporated Ni. *Chem. Eng. J.* **506**, 160048 (2025).
73. Sun, L. et al. Modulating the electronic structure of cobalt in molecular catalysts via coordination environment regulation for highly efficient heterogeneous nitrate reduction. *Angew. Chem. Int. Ed.* **63**, e202320027 (2024).
74. Daiyan, R. et al. Nitrate reduction to ammonium: from CuO defect engineering to waste NO_x-to-NH_3 economic feasibility. *Energ. Environ. Sci.* **14**, 3588–3598 (2021).
75. Yang, C. et al. Manipulating key intermediates and suppressing the hydrogen evolution reaction via dual roles of Bi for high-efficiency nitrate to ammonia and energy conversion. *Mater. Horiz.* **12**, 877–885 (2025).
76. Shahaf, Y., Slot, T. K., Avidan, S., Dick, J. E. & Eisenberg, D. Buffer effects on nitrite reduction electrocatalysis. *Acs Catal.* **15**, 7254–7262 (2025).
77. Fu, X. et al. Alternative route for electrochemical ammonia synthesis by reduction of nitrate on copper nanosheets. *Appl. Mater. Today* **19**, 100620 (2020).
78. Gao, Y. et al. Tandem catalysts enabling efficient C-N coupling toward the electrosynthesis of urea. *Angew. Chem.* **63**, e202402215 (2024).

79. Stagel, K., Ielo, L. & Bica-Schröder, K. Continuous synthesis of carbamates from CO_2 and amines. *ACS Omega* **8**, 48444–48450 (2023).
80. Mannisto, J. K. et al. Mechanistic insights into carbamate formation from CO_2 and amines: the role of guanidine–CO_2 adducts. *Catal. Sci. Technol.* **11**, 6877–6886 (2021).
81. Guo, P., Wang, X., Wang, Y., Luo, Y. & Chu, K. Electroreduction of CO_2 and nitrate for urea synthesis on a low-coordinated copper catalyst. *Chem. Commun.* **60**, 14649–14652 (2024).
82. Zhao, J. et al. Identifying the facet-dependent active sites of Cu_2O for selective C-N coupling toward electrocatalytic urea synthesis. *Appl. Catal. B Environ.* **340**, 123265 (2024).
83. Sulyaeva, V. S., Shayapov, V. R., Syrokvashin, M. M., Kozhevnikov, A. K. & Kosinova, M. L. Nano-sized copper films prepared by magnetron sputtering. *J. Struct. Chem.* **64**, 2438–2450 (2023).
84. Wang, M. et al. Tandem design on electrocatalysts and reactors for electrochemical CO_2 reduction. *Chin. J. Catal.* **69**, 1–16 (2025). (24)60209-3.
85. Lin, S.-W., Chao, J.-L., Ku, S.-C., Li, N. & Wu, A. T. Corrosion behaviors of Co, Co/Pd, and Co/Pd/Au surface finishes. *J. Taiwan Inst. Chem. Eng.* **138**, 104480 (2022).
86. Cohen, S. et al. A CoOxHy/β-NiOOH electrocatalyst for robust ammonia oxidation to nitrite and nitrate. *Green. Chem.* **25**, 7157–7165 (2023).
87. Gu, J. et al. Modulating electric field distribution by alkali cations for CO_2 electroreduction in strongly acidic medium. *Nat. Catal.* **5**, 268–276 (2022).
88. Chen, F.-Y. et al. Electrochemical nitrate reduction to ammonia with cation shuttling in a solid electrolyte reactor. *Nat. Catal.* **7**, 1032–1043 (2024).
89. Liu, S., Wang, Z., Qiu, S. & Deng, F. Mechanism in pH effects of electrochemical reactions: a mini-review. *Carbon Lett.* **34**, 1269–1286 (2024).
90. Haryanto, A., Jung, K., Lee, C. W. & Kim, D.-W. In situ infrared, Raman and X-ray spectroscopy for the mechanistic understanding of hydrogen evolution reaction. *J. Energy Chem.* **90**, 632–651 (2024).
91. Liang, C. et al. Role of Electrolyte pH on Water Oxidation for Iridium Oxides. *J. Am. Chem. Soc.* **146**, 8928–8938 (2024).
92. Kuhl, K. P., Cave, E. R., Abram, D. N. & Jaramillo, T. F. New insights into the electrochemical reduction of carbon dioxide on metallic copper surfaces. *Energ Environ. Sci.* **5**, 7050–7059 (2012).
93. Hori, Y. in *Modern Aspects of Electrochemistry Modern Aspects of Electrochemistry* Ch. 89–189 (2008).
94. Xiong, Y. et al. Electrochemical nitrate reduction: Ammonia synthesis and the beyond. *Adv. Mater.* **36**, 2304021 (2023).
95. Yang, J., Sebastian, P., Duca, M., Hoogenboom, T. & Koper, M. T. M. pH dependence of the electroreduction of nitrate on Rh and Pt polycrystalline electrodes. *Chem. Commun.* **50**, 2148–2151 (2014).
96. Zhang, R. et al. Electrochemical nitrate reduction in acid enables high-efficiency ammonia synthesis and high-voltage pollutes-based fuel cells. *Nat. Commun.* **14**, 8036 (2023).
97. Kas, R. et al. Electrochemical CO_2 reduction on Cu_2O-derived copper nanoparticles: controlling the catalytic selectivity of hydrocarbons. *Phys. Chem. Chem. Phys.* **16**, 12194–12201 (2014).
98. Liu, S. et al. Yttrium-doped NiMo-MoO_2 heterostructure electrocatalysts for hydrogen production from alkaline seawater. *Nat. Commun.* **16**, 773 (2025).
99. Haisch, T. et al. The origin of the hysteresis in cyclic voltammetric response of alkaline methanol electrooxidation. *Phys. Chem. Chem. Phys.* **22**, 16648–16654 (2020).
100. Karković Marković, A., Jakobušić Brala, C., Pilepić, V. & Uršić, S. Kinetic isotope effects and hydrogen tunnelling in PCET oxidations of ascorbate: new insights into aqueous chemistry? *Molecules* **25**, 1443 (2020).
101. Liu, J. et al. Optimizing the electronic structure of copper and cobalt dual sites for efficient electrosynthesis of urea. *Inorg. Chem. Front.* **12**, 3426–3437 (2025).
102. Huang, J. et al. Directly synthesized cobalt oxyhydroxide as an oxygen evolution catalyst in proton exchange membrane water electrolyzers. *Nat. Commun.* **16**, 7518 (2025).
103. Wang, J. et al. Sb incorporated into oxides enhances stability in acid during the oxygen evolution reaction by inhibiting structural distortion. *Nano Energy* **110**, 108355 (2023).
104. Zheng, P. et al. Detection of nitrite with a surface-enhanced Raman scattering sensor based on silver nanopyramid array. *Anal. Chim. Acta* **1040**, 158–165 (2018).
105. Sergent, N., Epifani, M., Comini, E., Faglia, G. & Pagnier, T. Interactions of nanocrystalline tin oxide powder with NO2: a Raman spectroscopic study. *Sens. Actuators B Chem.* **126**, 1–5 (2007).
106. Bisby, R. H., Johnson, S. A., Parker, A. W. & Tavender, S. M. Time-resolved resonance Raman spectroscopy of the carbonate radical. *J. Chem. Soc. Faraday Trans.* **94**, 2069–2072 (1998).
107. Xu, M. et al. Kinetically matched C–N coupling toward efficient urea electrosynthesis enabled on copper single-atom alloy. *Nat. Commun.* **14**, 6994 (2023).
108. Hadjiivanov, K. I. Identification of neutral and charged N_xO_y surface species by IR spectroscopy. *Catal. Rev.* **42**, 71–144 (2000).
109. Li, H., Wei, P., Gao, D. & Wang, G. In situ Raman spectroscopy studies for electrochemical CO_2 reduction over Cu catalysts. *Curr. Opin. Green Sustain. Chem.* **34**, 100589 (2022).
110. Liu, W.-P. et al. Effect of laser power on Raman analyses of lipids and amino acids: implications for extraterrestrial life exploration. *Icarus* **412**, 115986 (2024).
111. Li, X. et al. Selective visible-light-driven photocatalytic CO_2 reduction to CH_4 mediated by atomically thin $CuIn_5S_8$ layers. *Nat. Energy* **4**, 690–699 (2019).
112. Hu, Q. et al. Pulsed co-electrolysis of carbon dioxide and nitrate for sustainable urea synthesis. *Nat. Sustain* **7**, 442–451 (2024).
113. Han, S. et al. Ultralow overpotential nitrate reduction to ammonia via a three-step relay mechanism. *Nat. Catal.* **6**, 402–414 (2023).
114. Smith, B. C. Infrared spectral interpretation, in the beginning I: the meaning of peak positions, heights, and widths. *Spectroscopy* **39**, 18–24 (2024).
115. Guo, C. et al. Electrochemical upgrading of formic acid to formamide via coupling nitrite co-reduction. *J. Am. Chem. Soc.* **144**, 16006–16011 (2022).
116. Deng, Y., Handoko, A. D., Du, Y., Xi, S. & Yeo, B. S. In situ Raman spectroscopy of copper and copper oxide surfaces during electrochemical oxygen evolution reaction: identification of Cu^{III} oxides as catalytically active species. *ACS Catal.* **6**, 2473–2481 (2016).
117. Guda, A. A. et al. Understanding X-ray absorption spectra by means of descriptors and machine learning algorithms. *npj Comput. Mater.* **7**, 203 (2021).
118. Blaseio, S. et al. Impact of Cu^+ and Cu^{2+} species on the oxide-metal transition processes of Cu_xO foams during the CO_2RR probed by operando Quick-XAS. *J. Mater. Chem. A* **12**, 28177–28192 (2024).
119. Wang, J. et al. In situ X-ray spectroscopies beyond conventional X-ray absorption spectroscopy on deciphering dynamic configuration of electrocatalysts. *Nat. Commun.* **14**, 6576 (2023).
120. Zhang, Z. et al. Stable dual metal oxide matrix for tuning selectivity in acidic electrochemical carbon dioxide reduction. *Appl. Catal. B Environ. Energy* **371**, 125203 (2025).
121. Iijima, G., Inomata, T., Yamaguchi, H., Ito, M. & Masuda, H. Role of a hydroxide layer on Cu electrodes in electrochemical CO_2 reduction. *Acs Catal.* **9**, 6305–6319 (2019).
122. Luo, H., Li, B., Ma, J. G. & Cheng, P. Surface modification of nano-Cu_2O for controlling CO_2 electrochemical reduction to ethylene and syngas. *Angew. Chem. Int. Ed.* **61**, e202116736 (2022).

123. Kim, J. et al. Spatiotemporal active phase evolution for CO_2. *Electrocatal. Joule* **8**, 3373–3385 (2024).
124. Deng, Z. et al. High-efficiency electrochemical nitrate reduction to ammonia on a Co_3O_4 nanoarray catalyst with cobalt vacancies. *Acs Appl Mater. Inter* **14**, 46595–46602 (2022).
125. Mayer, J. M. Bonds over electrons: proton coupled electron transfer at solid–solution interfaces. *J. Am. Chem. Soc.* **145**, 7050–7064 (2023).
126. Yan, X., Zhuang, L., Zhu, Z. & Yao, X. Defect engineering and characterization of active sites for efficient electrocatalysis. *Nanoscale* **13**, 3327–3345 (2021).
127. Rodríguez, I. Harnessing artificial intelligence for modeling amorphous and amorphous porous palladium: A deep neural network approach. *MRS Commun.* **15**, 682–689 (2025).
128. Oh, S. et al. Porous Co–P foam as an efficient bifunctional electrocatalyst for hydrogen and oxygen evolution reactions. *J. Mater. Chem. A* **4**, 18272–18277 (2016).
129. El-Maghrabi, H. H. et al. Coaxial nanofibers of nickel/gadolinium oxide/nickel oxide as highly effective electrocatalysts for hydrogen evolution reaction. *J. Colloid Inter. Sci.* **587**, 457–466 (2021).
130. Ma, Z. et al. Reconstructing Cu nanoparticle supported on vertical graphene surfaces via electrochemical treatment to tune the selectivity of CO_2 reduction toward valuable products. *ACS Catal.* **12**, 4792–4805 (2022).
131. Huang, Y. M. et al. Unveiling the quantification minefield in electrocatalytic urea synthesis. *Chem. Eng.* **453**, 1–7 (2023).
132. King, H. J. et al. Photon-induced, timescale, and electrode effects critical for the in situ X-ray spectroscopic analysis of electrocatalysts: The water oxidation case. *J. Phys. Chem. C.* **123**, 28533–28549 (2019).
133. Kresse, G. & Furthmüller, J. Efficiency of ab-initio total energy calculations for metals and semiconductors using a plane-wave basis set. *Comput. Mater. Sci.* **6**, 15–50 (1996).
134. Kresse, G. & Furthmüller, J. Efficient iterative schemes for ab initio total-energy calculations using a plane-wave basis set. *Phys. Rev. B* **54**, 11169–11186 (1996).
135. Blöchl, P. E. Projector augmented-wave method. *Phys. Rev. B* **50**, 17953–17979 (1994).
136. Kresse, G. & Joubert, D. From ultrasoft pseudopotentials to the projector augmented-wave method. *Phys. Rev. B* **59**, 1758–1775 (1999).
137. Perdew, J. P., Burke, K. & Ernzerhof, M. Generalized gradient approximation made simple. *Phys. Rev. Lett.* **77**, 3865–3868 (1996).
138. Grimme, S., Antony, J., Ehrlich, S. & Krieg, H. A consistent and accurate ab initio parametrization of density functional dispersion correction (DFT-D) for the 94 elements H-Pu. *J. Chem. Phys.* **132**, 154104 (2010).

Acknowledgements

This research received funding from the Australian Research Council (ARC) Training Centre for Global Hydrogen Economy and supported by ARC Carbon Science and Innovation. We thank the NMR Facility at the Mark Wainwright Analytical Centre (MWAC), University of New South Wales, for providing NMR/EPR support, and the SSEAU surface analysis laboratory at MWAC for XPS assistance. We thank ANFF-ACT for providing facility and technical support to sample preparation. We acknowledge Electron Microscopy Unit (EMU) at MWAC and Adhi Satriyatama for the HRTEM analysis for post-reaction. We are also grateful for the in situ Raman spectroscopy support from the SPECLAB spectroscopy laboratory at MWAC. We gratefully acknowledge the Australian Synchrotron (ANSTO) for providing access to facilities and support. Parts of this work were carried out at the XAS (AS241/XAS/21410), MEX-1 (AS241/MEX1/21367), and IR (AS252/IRM/23927) beamlines under approved proposals. P.R. acknowledges the LPDP scholarship support from the Indonesian Finance Ministry (LPDP 202207220110457). R.K.H. gratefully acknowledges support from the Future Fellowship (FT230100054). R.D. and A.N.S. are thankful for the ARC's funding through the Discovery Early Career Researcher Award (DE230101396) and the Future Fellowship (FF200100317), respectively. R.D. acknowledges funding from UNSW Scientia Fellowship.

Author contributions

R.D., T.T.-P., A.N.S., and R.A. developed the concept and led the research effort. P.R. was responsible for conducting characterization, activity testing, and quantification of products. T.T.-P., X.M.C.T., and P.R. engaged in the catalyst synthesis, XRD characterization, and XPS fitting. P.R. performed the in situ SR-FTIR and MEX-1 measurements. P.R. conducted ex situ Raman analysis. P.R. and Z.M. executed the in situ Raman spectroscopy studies. P.R., R.K.H., T.T.-P., and B.J. conducted in situ synchrotron XAS measurements and their analysis. J.A.Y. and P.K. undertook density functional theory calculations. D.G. conducted the HRTEM and SAED analysis. The manuscript was co-written by P.R., T.T.-P., R.K.H., B.J., A.N.S., R.A., A.T., and R.D. All authors played a role in analyzing the results and contributing to the discussions.

Competing interests

The authors declare no competing interests.

Additional information

Supplementary information The online version contains supplementary material available at https://doi.org/10.1038/s41467-026-68481-6.

Correspondence and requests for materials should be addressed to Thành Trần-Phú or Rahman Daiyan.

Peer review information *Nature Communications* thanks the anonymous reviewers for their contribution to the peer review of this work. A peer review file is available.